Starbursts *in* and *out* of the star-formation main sequence

D. Elbaz[1], R. Leiton[2, 3, 1], N. Nagar[2], K. Okumura[1], M. Franco[1], C. Schreiber[4, 1], M. Pannella[5, 1], T. Wang[1, 6],
M. Dickinson[7], T. Díaz-Santos[8], L. Ciesla[1], E. Daddi[1], F. Bournaud[1], G. Magdis[9, 10], L. Zhou[1, 11], and
W. Rujopakarn[12, 13, 14]

[1] Laboratoire AIM-Paris-Saclay, CEA/DRF/Irfu - CNRS - Université Paris Diderot, CEA-Saclay, pt courrier 131, F-91191 Gif-sur-Yvette, France
   e-mail: `delbaz@cea.fr`
[2] Department of Astronomy, Universidad de Concepción, Casilla 160-C Concepción, Chile
[3] Instituto de Física y Astronomía, Universidad de Valparaíso, Avda. Gran Bretaña 1111, Valparaiso, Chile
[4] Leiden Observatory, Leiden University, NL-2300 RA Leiden, The Netherlands
[5] Fakultät für Physik der Ludwig-Maximilians-Universität, D-81679 München, Germany
[6] Institute of Astronomy, The University of Tokyo, 2-21-1 Osawa, Mitaka, Tokyo, 181-0015 Japan
[7] National Optical Astronomy Observatory, 950 North Cherry Avenue, Tucson, AZ 85719, USA
[8] Núcleo de Astronomía de la Facultad de Ingeniería, Universidad Diego Portales, Av. Ejército Libertador 441, Santiago, Chile
[9] Dark Cosmology Centre, Niels Bohr Institute, University of Copenhagen, Juliane Mariesvej 30, 2100, Copenhagen, Denmark
[10] Institute for Astronomy, Astrophysics, Space Applications and Remote Sensing, National Observatory of Athens, GR-15236 Athens, Greece
[11] School of Astronomy and Space Science, Nanjing University, Nanjing 210093, China
[12] Department of Physics, Faculty of Science, Chulalongkorn University, 254 Phayathai Road, Pathumwan, Bangkok 10330, Thailand
[13] National Astronomical Research Institute of Thailand (Public Organization), Donkaew, Maerim, Chiangmai 50180, Thailand
[14] Kavli Institute for the Physics and Mathematics of the Universe (WPI),The University of Tokyo Institutes for Advanced Study, The University of Tokyo, Kashiwa, Chiba 277-8583, Japan

ABSTRACT

Aims. We use high-resolution continuum images obtained with the Atacama Large Millimeter Array (ALMA) to probe the surface density of star-formation in $z{\sim}2$ galaxies and study the different physical properties between galaxies *within* and well above the star-formation main sequence of galaxies.
Methods. We use ALMA images at $870\,\mu m$ with 0.2 arcsec resolution in order to resolve star-formation in a sample of eight star-forming galaxies at $z{\sim}2$ selected among the most massive *Herschel* galaxies in the GOODS-*South* field. This sample is supplemented with eleven galaxies from the public data of the 1.3 mm survey of the Hubble Ultra-Deep Field, HUDF. We derive dust and gas masses for the galaxies, compute their depletion times and gas fractions and study the relative distributions of rest-frame UV and far-infrared light.
Results. ALMA reveals systematically dense concentrations of dusty star-formation close to the center of stellar component of the galaxies. We identify two different starburst regimes: *(i)* galaxies well above the SFR-$M_\star$ main sequence, with enhanced gas fractions, and *(ii)* a sub-population of galaxies located *within* the scatter of the main sequence that experience compact star formation with depletion timescales typical of local starbursts of ~150 Myr. In both starburst populations, the far infrared and UV are distributed in distinct regions and dust-corrected star formation rates estimated using UV-optical-NIR data alone underestimate the total star formation rate. In the starbursts above the main sequence, gas fractions are enhanced as compared to the main sequence. This may be explained by the infall of circum-galactic matter, hence by an enhanced conversion of total gas into stars. Starbursts *hidden* in the main sequence show instead the lowest gas fractions of our sample and could represent the late-stage phase of the merger of gas-rich galaxies, for which high-resolution hydrodynamic simulations suggest that mergers only increase the star formation rate by moderate factors. Active galactic nuclei are found to be ubiquitous in these compact starbursts, suggesting that the triggering mechanism also feeds the central black hole or that the active nucleus triggers star formation.

Key words. galaxies: evolution – galaxies: starburst – galaxies: active – galaxies: formation – galaxies: star formation – submillimeter: galaxies

1. Introduction

During the six billion years that have passed between a redshift of $z{\sim}2.5$ and 0.5, galaxies formed 75 % of their present stellar mass (see Fig.11 of Madau & Dickinson 2014) following a star-formation mode in which most of the UV starlight was absorbed by interstellar dust and re-radiated in the mid to far infrared (mid-IR and far-IR respectively, see e.g., Magnelli et al. 2009,

2013, Le Floc'h et al. 2005, Burgarella et al. 2013, Madau & Dickinson 2014 and references therein).

The galaxies that contributed most to the cosmic star formation rate (SFR) density therefore radiated most of their light in the infrared domain and at the peak epoch of cosmic star-formation, the so-called "cosmic noon" around $z{\sim}2$, these galaxies belonged to the class of luminous and ultraluminous infrared galaxies; LIRGs and ULIRGs, (U)LIRGs hereafter, with total

infrared luminosities of $L_{IR}=10^{11}-10^{12}$ L$_\odot$ and $L_{IR}>10^{12}$ L$_\odot$ respectively. It is therefore of prime importance to understand the star formation mode of $z\sim2$ dusty star-forming galaxies to trace back the origin of present-day stars and galaxies.

Contrary to their local siblings, the distant (U)LIRGs do not systematically exhibit the signature of merger-driven starbursts with compact star formation and depletion times of the order of $\sim$150 Myr. Instead, they appear to be in majority forming stars through a secular mode of star-formation (see e.g., Elbaz et al. 2010, 2011, Daddi et al. 2010b, Rujopakarn et al. 2011, Wuyts et al. 2011b) with depletion times, $\tau_d=M_{gas}$/SFR$\sim$600 Myr (Tacconi et al. 2017). Here τ_d is the time it would take for the galaxy to exhaust its molecular gas reservoir assuming a constant SFR. It is the inverse of the star formation efficiency, SFE. This evolution from a local population of rare violent merger-driven local (U)LIRGs to a common population of secularly evolving star-forming galaxies at $z\sim2$ is for the most part a natural result of the fast rise of the gas fraction of (U)LIRGs with increasing redshift (see e.g., Daddi et al. 2010a, Magdis et al. 2012b, Tacconi et al. 2010, 2017).

This change in the nature of (U)LIRGs as a function of cosmic time can also be seen in the framework of the global evolution of the correlation between the SFR and stellar mass followed by star-forming galaxies, the so-called "star-formation main sequence" (MS, hereafter). This tight correlation between the SFR and stellar mass (M$_\star$) is followed by the majority of star-forming galaxies from $z\sim0$ up to at least $z\sim3.5$ (Elbaz et al. 2007, Noeske et al. 2007, Daddi et al. 2007, Schreiber et al. 2015, 2017, Pannella et al. 2009, 2015, Karim et al. 2011, Wuyts et al. 2011a, Rodighiero et al. 2014, Whitaker et al. 2012, 2014, Renzini & Peng 2015). While the existence of a correlation between SFR and M$_\star$ is natural, the fact that 68 % of the star-forming galaxies of a given stellar mass formed their stars with the same SFR within a factor 2 (0.3 dex–*rms*) during 85 % of cosmic history (Schreiber et al. 2015) does appear as a surprise and a challenge for models.

This implies, in particular, that galaxies more massive than M$_\star=10^{10}$ M$_\odot$ were LIRGs and galaxies with M$_\star\geq1.4\times10^{11}$ M$_\odot$ were ULIRGs at $z\sim2$. (U)LIRGs therefore represented a common phase among distant massive galaxies and studying their nature is equivalent to studying the origin of massive galaxies. And indeed the studies of the dust and gas content of $z\sim2$ star-forming galaxies did reveal much longer typical depletion times for galaxies for MS galaxies at all masses, including (U)LIRGs at the high mass end of the MS which also present depletion times of about 600 Myr (Magdis et al. 2012b, Tacconi et al. 2017, Genzel et al. 2015, Béthermin et al. 2015).

The existence of a SFR – M$_\star$ MS is commonly used to disentangle a secular–universal star-formation mode of galaxies *within* the MS from a stochastic star-formation mode of galaxies *out* of the MS, in which *starbursts* systematically lie above the MS (see e.g., Rodighiero et al. 2011, Elbaz et al. 2011, Schreiber et al. 2015 and references therein). The fact that the proportion of starbursts – defined as galaxies experiencing star formation 3 or 4 times above the median of the MS SFR – remains limited to a few percent at all redshifts and masses (Rodighiero et al. 2011, Schreiber et al. 2015) is puzzling when one considers that the observed (e.g., Kartaltepe et al. 2007) and modeled (e.g., Hopkins et al. 2010) merger rate rapidly rises with increasing redshift.

What physical processes sustain the secular star-formation of the MS? What role did mergers play around cosmic noon? Are starbursts limited to the small population of galaxies with an extremely large specific SFR (sSFR=SFR/M$_\star$, e.g., Rodighiero et al. 2011) or can there be starbursts "hidden" within the MS?

Should one interpret the MS of star-forming galaxies as evidence that galaxies within it unequivocally form their stars following a common universal mode that is, in particular, unaffected by mergers?

We address these questions in this paper by taking advantage of the exquisite angular resolution of the Atacama Large Millimeter Array (ALMA). We use ALMA to probe the distribution of dusty star formation in $z\sim2$ (U)LIRGs and compare it with that derived from rest-frame UV light. We compare the spatial locations of UV-transparent and dusty star formation and discuss the presence or absence of spatial correlations between both with other galaxy properties, such as their depletion time and star-formation compactness. Here we identify a population of galaxies that lie *within* the MS but that exhibit enhanced star formation typical of starbursts – in terms of star-formation efficiency, SFE=SFR/M$_{gas}$, or equivalently depletion time, τ_{dep}=1/SFE. We consider several possible scenarios that may provide an explanation for the existence of these *starbursts hidden in the MS*, study a possible link with the presence of an active galactic nucleus (AGN) and discuss implications on the formation of compact early-type galaxies as observed at $z\sim2$ (e.g., van der Wel et al. 2014).

Throughout this paper we use a Salpeter (1955) initial mass function (IMF), and adopt a ΛCDM cosmology with $\Omega_M = 0.3$, $\Omega_\Lambda = 0.7$ and $H_0 = 70$ km s^{-1} Mpc^{-1} . As a matter of notation, we refer to the rest-frame GALEX far-ultraviolet (FUV) bandpass and to the total integrated IR light in the range 8–1000 μm when using the subscripts "UV" and "IR", respectively.

2. Data

An ensemble of 8 galaxies with *Herschel* photometry defines the core sample of this study for which deep 870 μm ALMA (band 7) continuum images were obtained (40–50 min on source, Cycle 1, P.I. R.Leiton). These galaxies are complemented with 11 galaxies observed at 1.3 mm from public ALMA data in the Hubble Ultra-Deep Field, HUDF ($\sigma_{1.3}\sim 35\,\mu$Jy; Dunlop et al. 2017, Rujopakarn et al. 2016). The resulting sample of 19 galaxies at $z\sim2$ is described below.

2.1. Sample selection

The main sample of galaxies used for this paper comes from the ALMA project 2012.1.00983.S (P.I.R.Leiton, Cycle 1) which was observed from August 29 to September 1st, 2014. It consists of eight $z\sim2$ ULIRGs (ultra-luminous infrared galaxies, L$_{IR}\geq10^{12}$ L$_\odot$) that were selected from a sample of *Herschel* galaxies detected in the GOODS-*South* field from the GOODS-*Herschel* open time key program (Elbaz et al. 2011).

These galaxies were selected in a way to avoid being heavily biased towards the minor population of starburst galaxies, well above the MS, but at the same time to reach a high enough signal-to-noise ratio in the high-resolution ALMA images at 870 μm (i.e., 290 μm rest-frame). The image quality and resolution were set with the goal of being able to determine the compactness and clumpiness of star-formation in these galaxies. This resulted in the requirements listed below that limited the sample to only 8 galaxies with a median stellar mass of M$_\star$=1.9$\times10^{11}$ M$_\odot$.

Starting from the GOODS-*Herschel* galaxy catalog (described in Elbaz et al. 2011), we selected the ALMA targets under the following conditions:

(i) a redshift – either spectroscopic or photometric – of 1.5<z<2.6 to ensure that the MIPS-24 μm band encompasses the

$8\,\mu$m wavelength to allow the determination of a rest-frame $8\,\mu$m luminosity, necessary to compute the *IR*8 color index. This color index, *IR*$8=L_{IR}/L_{8\mu m}$, was found to exhibit a tight correlation with the surface density of mid and far-infrared luminosity by Elbaz et al. (2011). Here $L_{8\mu m}$ is the νL_ν broadband luminosity integrated in the *Spitzer*–IRAC band 4 centered at $8\,\mu$m and L_{IR} is the total infrared luminosity integrated from 8 to $1000\,\mu$m. *IR*8 provides an independent tracer of dusty star formation compactness. This redshift encompasses the key epoch of interest here, the cosmic noon of the cosmic SFR density, and is large enough to bring the central wavelength, $870\,\mu$m, of ALMA band 7 (345 GHz) close to the peak of the far-infrared emission.

(ii) a sampling of the far infrared spectral energy distribution (SED) with measurements in at least four far-IR bands (100, 160, 250, $350\,\mu$m). This requirement is mainly constrained by the condition to have a 3–σ detection in the 250 and $350\,\mu$m bands together with the condition that the *Herschel*–SPIRE measurements are not heavily affected by contamination from close neighbors. The latter condition is determined through the use of a "clean index" (defined in Elbaz et al. 2010, 2011). The clean index is used to reject sources with highly uncertain flux densities due to confusion by only selecting sources with at most one neighbor closer than $0.8\times$FWHM($250\,\mu$m)$=18''$ and brighter than half the $24\,\mu$m flux density of the central object. This was done using the list of sources detected at $24\,\mu$m above $20\,\mu$Jy. Simulations using realistic infrared SED and galaxies spatial distributions together with the *Herschel* noise showed that this criterion ensures a photometric accuracy better than 30 % in at least 68 % of the cases for SPIRE detections (Leiton et al. 2015).

(iii) we rejected sources with unphysical SED, i.e., for which one or more of the flux densities from 24 to $350\,\mu$m presented a non physical jump. This smoothness condition on the SED was required to reject sources with blending effects, affecting mainly the longest *Herschel* wavelengths even after imposing the clean index criterion.

For the sake of simplicity, we labeled the eight sources GS1 to GS8. We also provide their CANDELS ID, ID_{CLS}, from Guo et al. (2013) in Table 1. We note that all of the *Herschel* sources studied here were found to be associated with a single ALMA source, none was split into two or more ALMA sources.

2.2. Supplementary sample from the Hubble Ultra Deep Field

We supplemented our sample with a reference sample of galaxies detected with ALMA at 1.3 mm with a resolution of $\sim$0.35 arcsec within the 4.5 arcmin^2 survey of the Hubble Ultra Deep Field (HUDF) down to $\sigma_{1.3}\sim 35\,\mu$Jy (see Dunlop et al. 2017, Rujopakarn et al. 2016). We use here the 11 galaxies listed in the Table 2 of Rujopakarn et al. (2016) (see Section 2.3). The galaxies are labeled UDF# in Table 1 as in Dunlop et al. (2017).

2.3. ALMA observations and data reduction

2.3.1. ALMA observations

Each one of the eight targeted galaxies was observed with a single pointing with a total of 36 antennas in band 7 (345 GHz, $870\,\mu$m) at an angular resolution of $0.2''$(ALMA synthesized beam of $0.2''\times0.16''$). The integration time on each science target ranges from 37 to 50 minutes, resulting in typical signal-to-noise ratios at $870\,\mu$m of S/N$\sim$35 and up to 75 for the brightest one. The integration time was defined in order to reach a minimum S/N=10 on 20 % of the predicted $870\,\mu$m ALMA flux den-

Table 1. ALMA sources.

ID	ID_{CLS}	Ra$_{CLS}$, Dec$_{CLS}$ 3h32m...,−27°...	offset *arcsec*
(1)	(2)	(3)	(4)
GS1	3280	43.33s , 46′56.73″	0.176,−0.188
GS2	5339	34.44s , 46′40.74″	0.052,−0.232
GS3	2619	36.98s , 47′25.88″	0.083,−0.173
GS4	7184	41.03s , 46′37.35″	0.161,−0.280
GS5	9834	43.53s , 46′16.28″	0.089,−0.248
GS6	14876	38.55s , 46′58.41″	0.091,−0.269
GS7	8409	39.74s , 46′00.63″	0.067,−0.225
GS8	5893b	44.03s , 46′21.31″	0.081,−0.184
UDF1	15669	44.03s , 46′35.98″	0.066,−0.277
UDF2	15639	43.53s , 46′39.28″	0.057,−0.277
UDF3	15876	38.55s , 46′34.31″	0.083,−0.243
UDF4	15844	41.03s , 46′31.70″	0.063,−0.250
UDF5	13508	36.98s , 47′27.44″	0.101,−0.239
UDF6	15010	34.44s , 46′59.82″	0.100,−0.254
UDF7	15381	43.33s , 46′47.05″	0.050,−0.250
UDF8	16934	39.74s , 46′11.54″	0.043,−0.289
UDF11	12624	40.06s , 47′55.70″	0.090,−0.242
UDF13	15432	35.08s , 46′47.84″	0.098,−0.260
UDF16	14638	42.38s , 47′07.85″	0.069,−0.242

Notes: The upper part of the table lists the 8 galaxies (GS1 to GS8) observed with ALMA at $870\,\mu$m at a 0.2 arcsec resolution in our ALMA program. The lower part lists the 11 galaxies (UDF#) from the 1.3mm ALMA survey of the HUDF by Dunlop et al. (2017) at a resolution of 0.35 arcsec. Col.(1) Simplified ID. For the UDF galaxies, we use the same IDs as in Dunlop et al. (2017). Cols.(2) and (3) CANDELS ID and coordinates from Guo et al. (2013). GS8, initially associated with the galaxy with the CANDELS ID 5893, was found to be associated with a background galaxy that we will call 5893b (see Section 3.1). Col.(4) offset to be applied to the *HST* CANDELS coordinates to match the ALMA astrometry.

sity (extrapolated from *Herschel*) or equivalently 50-σ on the total flux in order to be able to measure an effective radius even for the most compact galaxies and to individually detect the major clumps of star formation when they exist and produce at least 20 % of the total ALMA flux density. For the typical predicted flux density of F$_{870}\sim$2.5 mJy of the sample, this led to a total observing time of at least 35 minutes/object. Accounting for the predicted flux densities of the galaxies, we used slightly different integration times of 36.5, 38.8 and 49.5 minutes (excluding overheads) for [GS4, GS5, GS6, GS8], [GS1, GS7] and [GS2, GS3] respectively. The observed standard deviation of the noise spans *rms*=40-70 μJy. Accounting for the obtained S/N, the accuracy on the size measurements given by CASA corresponds to FWHM/$\sqrt{(S/N)}\sim$0.034 arcsec that represents a theoretically expected precision, if we assume that the sources have a Gaussian profile, corresponding to $\sim$280 pc at $z\sim$2.

2.3.2. Data reduction, flux and size measurements

The data reduction was carried out with CASA, and the final images were corrected for the primary beam, although all our targets are located at the center of the ALMA pointings. Flux densities and sizes were both measured in the *uv* plane, using the *uvmodelfit* code in CASA, and in the image plane using the *GALFIT* code (Peng et al. 2002). Since *uvmodelfit* only allows 2D Gaussian profile fitting, we computed Gaussian and Sérsic

profiles with *GALFIT* to compare both results. The Gaussian semi-major axis ($R_{1/2}$=0.5×FWHM of the major axis) derived in the *uv* and image planes – with *uvmodelfit* and *GALFIT* respectively – agree within 15 %, with only a 5 % systematic difference (larger sizes in the *GALFIT* measurements in the image plane). However, the uncertainties estimated by *GALFIT* in the image plane are 45 % smaller (median, with values that can reach more than a factor 2). We consider that the uncertainties measured in the *uv* plane are most probably more realistic, and anyway more conservative, hence we have decided to use the *uvmodelfit* measurements for our analysis (see Table 2).

We compared the Gaussian semi-major axis from *uvmodelfit*, $R_{1/2}$, with the effective radius, R_e, obtained with a Sérsic profile fit either leaving the Sérsic index free, n_{ALMA}^{Sersic}, or imposing n_{ALMA}^{Sersic}=1 (exponential disk profile). We find that $R_{1/2}$ and R_e agree within 20 % in both cases with no systematic difference when imposing n_{ALMA}^{Sersic}=1 and 4 % smaller sizes when the Sérsic index is left free. We obtain a S/N ratio greater than 3 for the Sérsic indices (Col.(7) in Table 2) of all the GS sources except GS2 and GS3 (ID CANDELS 5339 and 2619).

Hence even though we did perform Sérsic profil fittings and determined n_{ALMA}^{Sersic}, the light distribution of our galaxies does not seem to show very strong departure from a 2D Gaussian. As a result both $R_{1/2}$ and R_e provide an equally good proxy for the half-light radius, encompassing 50 % of the IR luminosity. We did measure some moderate asymmetries quantified by the minor (*b*) over major (*a*) axis ratio, *b/a* (Col.(5) in Table 2) that we used to derive circularized half-light radii, R_{ALMA}^{circ} (listed in kpc in the Col.(6) of Table 2) following Eq. 1.

$$R_{ALMA}^{circ}[\text{kpc}] = R_{1/2} \times \sqrt{\frac{b}{a}} \times \text{Conv}(''\text{ to kpc}) \qquad (1)$$

Conv($''$ to kpc) is the number of proper kpc at the redshift of the source and is equal to 8.46, 8.37 and 8.07 kpc/$''$ at z=1.5, 2 and 2.5 respectively. We then used R_{ALMA}^{circ} – that encompasses 50 % of the IR luminosity – to compute the IR luminosity surface densities of our galaxies as in Eq. 2.

$$\Sigma_{\text{IR}}[\text{L}_\odot \text{ kpc}^{-2}] = \frac{L_{\text{IR}}/2}{\pi(R_{ALMA}^{circ})^2} \qquad (2)$$

The sizes of the HUDF galaxies were measured as well using a 2D elliptical Gaussian fitting by Rujopakarn et al. (2016) who used the PyBDSM[1] code. We analyzed the public ALMA image of the HUDF and found that the quality of the images did not permit to constrain both a Sérsic effective radius and index, hence we do not provide Sérsic indices for the HUDF galaxies. We fitted with *GALFIT* 2D Gaussian elliptical profiles on the 11 HUDF sources listed in Rujopakarn et al. (2016) and found a good agreement between our measured Gaussian FWHM values and those quoted in Rujopakarn et al. (2016) with a median ratio of exactly 1 and an *rms* of 16 % for the sources with S/N>5. Below this threshold, the measured sizes agree within the error bars which start to be quite large. We quote in Table 2 the sizes listed in Rujopakarn et al. (2016).

The flux densities of the GS galaxies were computed using our 2D elliptical Gaussian fitting in the *uv* plane. For the HUDF galaxies, they correspond to those listed in Rujopakarn et al. (2016) consistent with our own measurements.

---

[1] http://www.astron.nl/citt/pybdsm
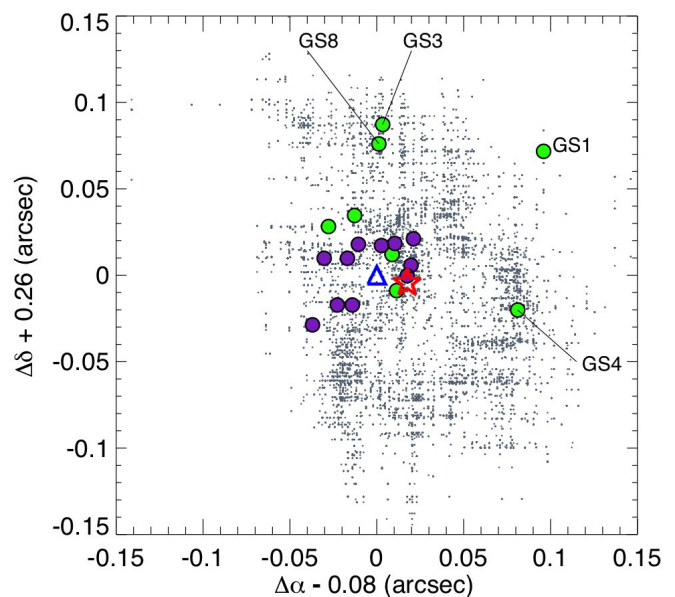
Fig. 1. Astrometric offsets to be applied to the positions of the CAN-DELS HST catalog in GOODS-*South* to match the positions of the sources detected in Pan-STARRS1 (small grey dots). We centered the diagram on the systematic astrometric correction of [0.08$''$, −0.26$''$] introduced by Dunlop et al. (2017) and Rujopakarn et al. (2016) for the HUDF, marked by an open blue triangle. The open red star marks the median of the systematic astrometric correction over the whole 10′×15′ GOODS-*South* field [0.095$''$, −0.264$''$]. A detailed description of these astrometric offsets will be provided in Dickinson et al. (in prep.). The large green and purple dots mark the 8 GS sources and 11 UDF sources detected with ALMA at 870 μm and 1.3mm respectively.

2.3.3. ALMA vs *HST* astrometry

The ALMA and *HST* coordinates present a small systematic offset in the GOODS-*South* field. This offset does not exist between ALMA and other observatories such as 2MASS, JVLA, GAIA or Pan-STARRS but it affects the astrometry of the *HST* sources. A comparison of the positions of *HST* sources in the HUDF with 2MASS (Dunlop et al. 2017) and JVLA (Rujopakarn et al. 2016) showed that the *HST* positions needed to be corrected by −0.26 arcsec in Declination and +0.08 arcsec in Right Ascension. This implies that the *HST* coordinates (in decimal degrees) must be systematically corrected by [+2.51,−7.22] ×10^{-5} degree (including the cos(δ) factor).

This offset is too small to change the *HST* counterparts of the ALMA detections. However, it has an impact on the detailed comparison of the location and shape of the ALMA millimeter emission with that of the *HST* optical light that will be discussed in the following sections. Hence we decided to extend further our analysis of this astrometric issue by searching for possible local offsets added to the global one mentioned above. A detailed description of the resulting analysis will be presented in Dickinson et al. (in prep.). We just briefly summarize here the main lines of this process and its implications on our analysis.

The main reasons for this astrometric issue can be traced back to the astrometric references that were used to build the *HST* mosaics of the GOODS-*South* field. At the time, the astrometric reference used for GOODS-*South* was an ESO 2.2m Wide Field Imager (WFI) image, itself a product of a combination of different observing programs (the ESO Imaging Survey, EIS and COMBO-17 among others). The GOODS *HST* team

Table 2. Galaxy properties derived from the ALMA and *HST*–WFC3 *H* band (1.6 μm) data.

ID	z	F_{ALMA} (μJy)	$R_{1/2maj}$ (arcsec)	b/a	R_{ALMA}^{circ} (kpc)	n_{ALMA}^{Sersic}	R_{H}^{circ} (kpc)	n_{H}^{Sersic}	$\Sigma_{IR}^{(a)}$ (×10^{11}L$_\odot$kpc^{-2})	$IR8$
(1)	(2)	(3)	(4)	(5)	(6)	(7)	(8)	(9)	(10)	(11)
GS1	2.191	1190 ± 120	0.145 ± 0.016	0.72	0.87±0.09	0.63±0.18	0.73	3.75	3.73 ± 1.00	9.3 ± 0.8
GS2	2.326	1100 ± 70	0.163 ± 0.031	0.87	1.16±0.22	1.07±0.99	1.90	0.72	2.63 ± 1.21	7.2 ± 0.9
GS3	2.241	1630 ± 70	0.150 ± 0.016	0.42	0.52±0.05	4.69±1.65	2.81	2.03	14.96 ± 3.90	8.1 ± 0.6
GS4	1.956^{sp}	2100 ± 70	0.140 ± 0.010	0.82	0.97±0.07	1.88±0.59	3.93	1.77	3.54 ± 0.81	13.4 ± 1.8
GS5	2.576^{sp}	4420 ± 70	0.139 ± 0.006	0.92	1.03±0.04	1.27±0.22	2.57	1.08	10.12 ± 1.38	–
GS6	2.309^{sp}	5210 ± 70	0.120 ± 0.004	1.00	0.98±0.03	1.15±0.21	2.10	0.25	10.86 ± 1.27	27.3 ± 2.4
GS7	1.619^{sp}	2320 ± 70	0.194 ± 0.012	0.84	1.38±0.09	1.78±0.38	3.66	1.04	2.33 ± 0.41	19.8 ± 1.7
GS8	3.240	6420 ± 140	0.142 ± 0.003	0.62	0.67±0.02	0.67±0.04	1.63	3.53	20.86 ± 2.25	–
UDF1	3.000	924 ± 76	0.195 ± 0.020	0.85	1.24±0.18	–	0.54	7.16	5.95 ± 2.00	–
UDF2	2.794^{sp}	996 ± 87	0.265 ± 0.030	0.85	1.77±0.18	–	3.24	0.86	1.32 ± 0.33	–
UDF3	2.543^{sp}	863 ± 84	0.375 ± 0.045	0.36	1.59±0.27	–	1.55	0.81	3.35 ± 1.28	9.9 ± 0.9
UDF4	2.430	303 ± 46	0.270 ± 0.060	0.52	1.42±0.35	–	2.79	0.20	0.84 ± 0.47	7.9 ± 1.3
UDF5	1.759^{sp}	311 ± 49	0.480 ± 0.125	0.20	1.59±0.62	–	2.24	0.71	0.48 ± 0.40	7.2 ± 0.7
UDF6	1.411^{sp}	239 ± 49	0.530 ± 0.205	0.19	1.77±1.06	–	3.71	0.48	0.46 ± 0.58	–
UDF7	2.590	231 ± 48	*0.120 ± 0.060*	–	*2.65±1.33*	–	4.24	0.77	*0.25 ± 0.27*	–
UDF8	1.546^{sp}	208 ± 46	0.675 ± 0.225	0.53	3.81±1.24	–	5.57	3.04	0.11 ± 0.08	4.7 ± 0.4
UDF11	1.998^{sp}	186 ± 46	0.715 ± 0.285	0.48	3.72±1.50	–	4.40	1.41	0.26 ± 0.22	6.4 ± 0.5
UDF13	2.497^{sp}	174 ± 45	0.430 ± 0.170	0.55	2.30±0.97	–	1.14	1.86	0.22 ± 0.20	6.9 ± 1.3
UDF16	1.319^{sp}	155 ± 44	*0.115 ± 0.058*	–	*2.74±1.37*	–	3.15	2.16	*0.07 ± 0.07*	–

Notes: Col.(1) Simplified ID. Col.(2) photometric redshift, except for the galaxies marked with $^{(sp)}$ for which a spectroscopic redshift is available. Col.(3) F_{ALMA} is the continuum flux density at 870 μm for the GS1 to GS8 sources and at 1.3mm for the UDF1 to UDF16 sources. Cols.(4) and (5) Semi-major axis, $R_{1/2maj}$ in arcsec, and axis ratio, b/a, of the ALMA sources measured from *uvmodelfit* in CASA for the GS sources and from Rujopakarn et al. (2016) for the UDF galaxies. The consistency of the GS and UDF was checked in the direct images using *GALFIT*. The sizes of UDF7 and UDF16 (in italics) are measured at the 2-σ level. Col.(6) circularized effective ALMA radius, R_{ALMA}^{circ}, in kpc, as defined in Eq. 1. Col.(7) Sérsic index, n_{ALMA}^{Sersic}, derived from the Sérsic fit to the ALMA 870 μm image for the GS sources using *GALFIT* on the direct images. The S/N of the UDF sources is not high enough to allow the fit of a Sérsic index. Cols.(8) and (9) are the circularized effective Sérsic radius, R_{H}^{circ} in kpc, and index, n_{H}^{circ}, derived from the Sérsic fit to WFC3 *H* band images by van der Wel et al. (2012). Col.(10) IR surface density in L$_\odot$kpc^{-2}, Σ_{IR}=(L_{IR}/2)/[π(R_{ALMA}^{circ})^2], where L_{IR} is given in Table 3 and R_{ALMA}^{circ} in Col.(6). Col.(11) $IR8$=L_{IR}/$L_{8\mu m}$ color index. The 8 μm rest-frame luminosities were derived from the observed *Spitzer*-MIPS 24 μm photometry as in Elbaz et al. (2011). $L_{8\mu m}$, hence also $IR8$, can only be determined from the observed 24 μm luminosity for galaxies with 1.5≤z≤2.5.

subsequently re-calibrated the WFI astrometry to match the *HST* Guide Star Catalog (GSC2).

More modern astrometric data are now available in this field such as Pan-STARRS1 (Chambers et al. 2016). We used the PanStarr DR1 catalogue provided by Flewelling et al. (2016) to search for possible offsets in the different regions of the whole 10′×15′ GOODS-*South* field.

We found residual distortions that we believe to be due to some combination of distortions in the WFI mosaic images and in the GSC2 positions, and zonal errors registering the *HST* ACS images to the WFI astrometry. These residual local distortions are plotted in Fig. 1 after having corrected the *HST* positions for the global offset mentioned above and marked with the open blue triangle. The distortion pattern was determined using a 2.4 arcmin diameter circular median determination of the offset in order to avoid artificial fluctuations due to the position uncertainty on the individual objects. This pattern was then applied to the 34,930 *HST* WFC3-*H* sources of the CANDELS catalog in GOODS-*South* (Guo et al. 2013; shown as grey dots in Fig. 1).

The 11 galaxies detected by ALMA in the HUDF are all well centered on this position with residual offsets of the order of 0.02″(large filled purple dots). These extra corrections are truly negligible, since they correspond to 160 pc at the redshifts of the sources. However, the 8 GS galaxies are spread over a wider area in GOODS-*South* including parts where the residual offsets can

be as large as ∼0.07″, i.e., 0.6 kpc. This is the case of GS1, GS3, GS4 and GS8.

We found that these local offsets did not not affect the associations with optical counterparts and that they were smaller than the difference between the positions of the rest-frame UV and FIR light distributions that we discuss in the following sections. Except in the case of the galaxy GS4, where the peak of the ALMA emission presented an offset with respect to the *HST*-WFC3 *H*-band centroid before applying the local correction for the *HST* astrometry and fell right on the *H*-band center after correction.

2.4. Dust, gas and stellar masses

The ALMA sources were cross-matched with the catalog of GOODS-*Herschel* sources described in Elbaz et al. (2011). All of the sources discussed in the present paper are detected with both *Herschel* photometers PACS and SPIRE with a S/N>3. The 8 GS sources are detected in the two PACS bands and at 250 and 350 μm with SPIRE (including 3 at 500 μm). The 11 UDF sources are detected in the PACS-160 μm and SPIRE-250 μm bands, 9 are detected at 100 μm, 7 at 350 μm and 2 at 500 μm. The 500 μm is obviously mainly limited by the large beam size at this wavelength with *Herschel* that imposes a hard confusion limit.
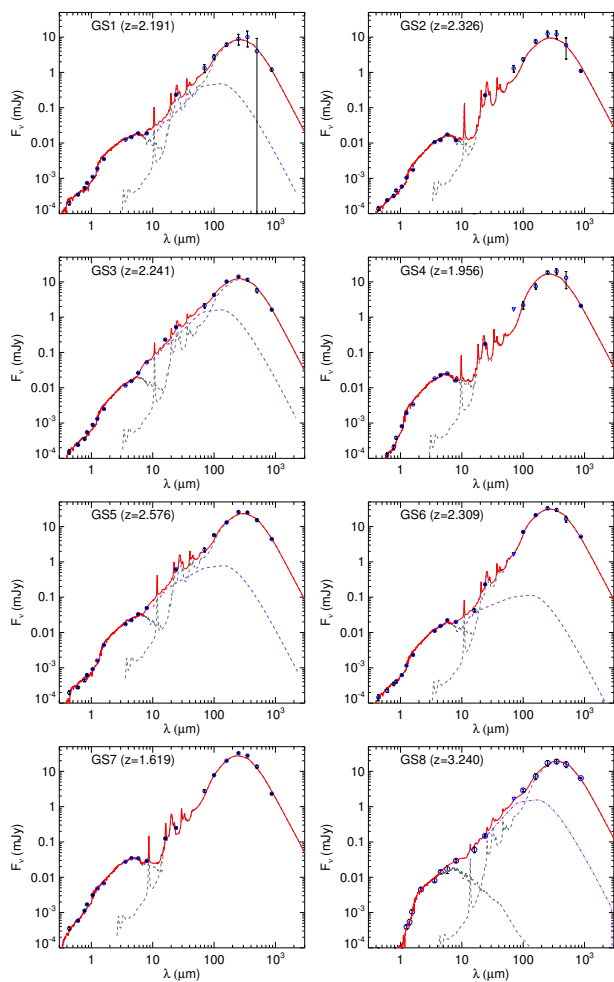
Fig. 2. Spectral energy distributions (SEDs) of the 8 GS galaxies. The solid red line shows the combination of the model fit of the *(i)* optical-NIR side of the SEDs done with the FAST code, *(ii)* IR energy distribution from the best-fitting Draine & Li (2007) model and when necessary (blue dashed line), *(iii)* the warm dust continuum heated by an AGN using the Mullaney et al. (2011) code *decompIR* (purple dashed line). The specific case of GS8 for which the optical counterpart is nearly undetected is discussed in Section 3.1.

The full SEDs including the optical, near-IR, mid-IR, far-IR and sub-millimeter flux densities of the 8 GS galaxies are presented in Fig. 2 together with spectral model fits to the data. The fit of the stellar side of the galaxies was used to determine their photometric redshifts with the EAzY[2] code (Brammer et al. 2008) and stellar masses with the FAST[3] code that is compatible with EAzY (see the Appendix of Kriek et al. 2009). For the galaxies with spectroscopic redshifts (GS4, GS5, GS6 and GS7), we computed the stellar masses at these spectroscopic values. The case of GS8 is peculiar and will be discussed in detail in Section 3.1.

For the UDF galaxies, we used the same redshifts as Dunlop et al. (2017) and Rujopakarn et al. (2016) for consistency. We present their dust SEDs in Fig. 3. We computed the stellar masses of the UDF galaxies at those redshifts.

Following Pannella et al. (2015), stellar masses were computed using a delayed exponentially declining star formation history with the Bruzual & Charlot (2003) stellar population synthe-
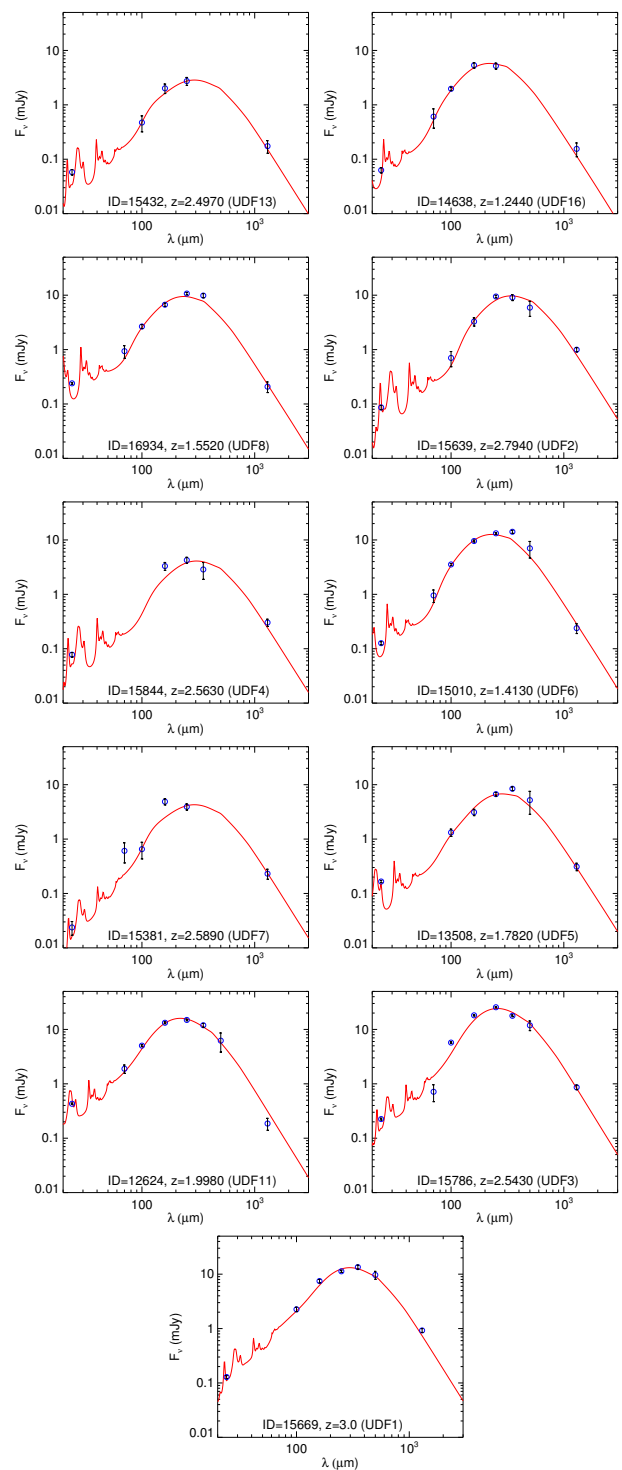
Fig. 3. Mid-IR to sub-millimeter SEDs of the 11 UDF galaxies fitted by the best-fitting IR energy distribution from Draine & Li (2007).
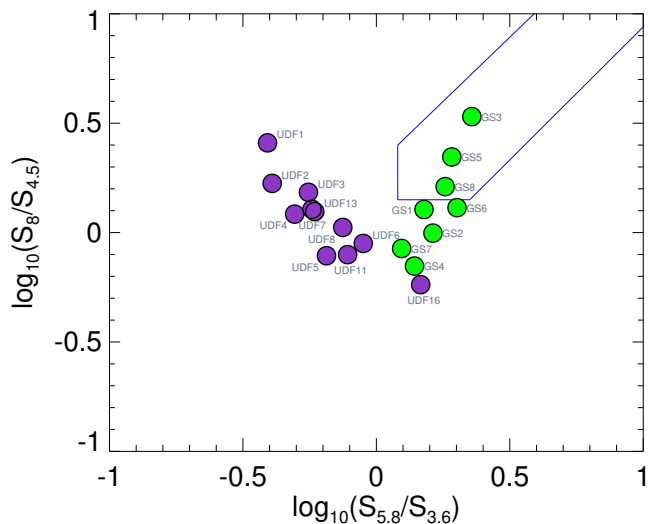
sis model to fit the observed photometry up to the IRAC $4.5\,\mu$m band. We assumed a solar metallicity, a Salpeter (1955) IMF and a Calzetti et al. (2000) attenuation law with A_V ranging from 0 to 4.

The dust side of the SED of the galaxies (from the *Spitzer* IRS-$16\,\mu$m and MIPS-$24\,\mu$m to the ALMA flux densities) was modeled using the IR emission spectra for dust heated by stellar light from Draine & Li (2007) by running the code CIGALE[4]

---

[2] Publicly available at http://www.github.com/gbrammer/eazy-photoz
[3] Publicly available at http://astro.berkeley.edu/ mariska/FAST.html

[4] Publicly available at http://cigale.lam.fr

Fig. 4. Mid-IR color-color diagram to search for potential power-law AGNs. Galaxies within the solid blue line are considered as candidate power-law AGNs by Donley et al. (2012).

Fig. 5. SFR – $M_\star$ main sequence at $1.5<z<2.5$ as measured in GOODS-*South*. Blue dots: $\mathrm{SFR_{SED}}$ derived from UV-optical-NIR SED fitting. Orange dots: $\mathrm{SFR_{tot}} = \mathrm{SFR_{IR}} + \mathrm{SFR_{UV}}$. In order to keep the relative position of each galaxy with respect to the main sequence at its redshift, the SFR was multiplied by $\mathrm{SFR^z_{MS}/SFR^{z=2}_{MS}}$ using Eq.9 from Schreiber et al. (2015). The 8 GS and 11 UDF ALMA sources discussed in this paper are shown with green and purple filled symbols respectively.

(Noll et al. 2009). Following Draine et al. (2007), we fixed the slope of the distribution of intensities of the interstellar radiation field (ISRF, U), α, to $\alpha=2$ and adopted an upper limit of $U_{max}=10^6~U_\odot$ for the ISRF in units of the solar ISRF.

The best-fitting SED was used to determine for each galaxy its total dust emission, L_{IR}, and a dust mass, M_{dust}, listed in Table 3. To derive a gas mass, we determined the total gas-to-dust ratio ($\delta_{GDR}=M_{gas}/M_{dust}$) using Eq. 3 from Leroy et al. (2011) (given in the text of their Section 5.2) that links δ_{GDR} with metallicity for local galaxies, hence assuming that this relation holds at all redshifts.
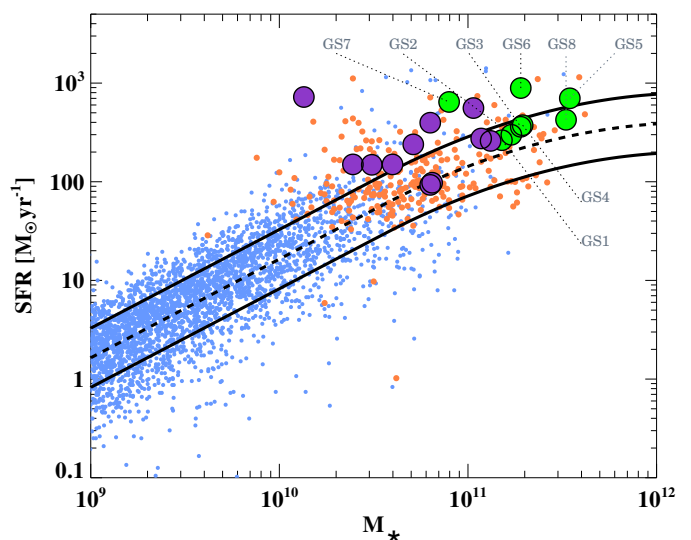
$$
\begin{aligned}
\log_{10}(\delta_{GDR}) &= \log_{10}\left(\frac{M_{HI}+M_{H_2}}{M_{dust}}\right) \\
&= (9.4 \pm 1.1) - (0.85 \pm 0.13)\,[12 + \log_{10}(O/H)]
\end{aligned}
$$
(3)

Metallicities for our $z\sim2$ sample of ALMA galaxies were inferred using the mass - metallicity relation described in Eq. 4 taken from Genzel et al. 2012 (see their Section 2.2) for galaxies at $z=1.5-3$, based on a combination of datasets including the data of Erb et al. (2006).

$$
\begin{aligned}
&12 + \log_{10}(O/H) = \\
&-4.51 + 2.18\,\log_{10}(M_\star/1.7) - 0.0896\,[\log_{10}(M_\star/1.7)]^2
\end{aligned}
$$
(4)

We replaced $M_\star$ in Eq. 4 by $M_\star/1.7$ since Genzel et al. (2012) used a Chabrier IMF whereas we are here using a Salpeter IMF ($M_\star^{Chabrier}=M_\star^{Salpeter}/1.7$).

Three galaxies are classified as power-law active galactic nuclei (AGN) following the color-color diagram definition of Donley et al. (2012) (blue solid line in Fig. 4): GS3, GS5 and GS8. We used the code *decompIR* by Mullaney et al. (2011) to subtract AGN contributions for all the galaxies. *decompIR* consistently identified an AGN contribution at $8\,\mu m$ for the three power-law AGNs and at a lower level for the galaxies GS1 and GS6 which stand very close to the limit of Donley et al. (2012) and for which the code *decompIR* found a small contribution. For all the other galaxies, *decompIR* did not find any noticeable AGN contribution. The AGN component (shown with the purple dashed line in Fig. 2) was subtracted from the data in a first iteration. We then

applied the CIGALE code to fit the residual emission and determine L_{IR} and M_{dust} free from any AGN contamination. We note however that both values are little affected by this AGN emission that mostly contributes to the mid-IR spectral range. Finally we note that we also applied an AGN correction for

2.5. Star formation rates and position on the star formation main sequence

The total SFR of the galaxies is defined as the sum of the IR ($\mathrm{SFR_{IR}}$) and uncorrected UV ($\mathrm{SFR_{UV}}$) SFR, $\mathrm{SFR_{tot}}=\mathrm{SFR_{IR}}+\mathrm{SFR_{UV}}$. $\mathrm{SFR_{IR}}$ and $\mathrm{SFR_{UV}}$ were computed following the conversions of Kennicutt (1998) and Daddi et al. (2004) given in Eq. 5 and Eq.6; where L_{UV} is the rest-frame 1500 Å UV luminosity computed from the best-fitting template obtained with EAzY (uncorrected for attenuation) and L_{IR} is the total dust luminosity given by the best-fitting Draine & Li (2007) model (see Section 2.4).

$$\mathrm{SFR_{IR}}~[M_\odot~yr^{-1}] = 1.72 \times 10^{-10} \times L_{IR}~[L_\odot]$$
(5)

$$\mathrm{SFR_{UV}}~[M_\odot~yr^{-1}] = 2.17 \times 10^{-10} \times L_{UV}~[L_\odot]$$
(6)

We also computed $\mathrm{SFR_{SED}}$ by fitting the rest-frame UV-optical-NIR data assuming a constant star formation history and a Calzetti et al. (2000) reddening law (Col.(5) in Table 3). This $\mathrm{SFR_{SED}}$ will be compared to $\mathrm{SFR_{tot}}$ in order to determine the presence of residual dust attenuation unaccounted for by the UV-optical SED fitting. To derive $\mathrm{SFR_{SED}}$, we limited ourselves to a constant SFR history in order to avoid the degeneracy between dust attenuation and stellar population ages. Rest-frame magnitudes were computed from the best-fit SED model integrated through the theoretical filters by running EAZY on the multi-wavelength catalog. The resulting $\mathrm{SFR_{tot}}$ and $\mathrm{SFR_{SED}}$ are listed

Table 3. Integrated properties of the ALMA sources.

ID	SM	L_{IR} ($\times 10^{11} L_\odot$)	SFR_{tot} ($M_\odot yr^{-1}$)	SFR_{SED} ($M_\odot yr^{-1}$)	$log_{10}(M_\star)$ ($M_\odot$)	R_{SB}	$log_{10}(L_X)$ (erg.s^{-1})	$M_{dust}^{(a)}$ ($\times 10^8 M_\odot$)	$M_{gas}^{(a)}$ ($\times 10^{10} M_\odot$)	τ_{dep} (Myr)
(1)	(2)	(3)	(4)	(5)	(6)	(7)	(8)	(9)	(10)	(11)
GS1	S	17.6±0.9	306±15	107	11.18	1.39	43.44	4.2±0.4	4.9±0.5	161±24
GS2	S	22.2±1.9	385±32	100	11.23	1.47	–	5.1±0.5	6.0±0.6	156±28
GS3	S	25.3±1.3	438±22	112	11.28	1.66	43.44	5.5±0.3	6.3±0.3	144±14
GS4	S	20.9±1.8	360±31	290	11.29	1.70	–	8.2±1.1	9.3±1.3	258±57
GS5	S	66.8±3.3	1154±57	339	11.54	2.41	43.54	14.5±0.7	15.1±0.8	131±13
GS6	M	66.1±3.3	1139±57	107	11.28	4.10	42.29	15.7±1.2	17.9±1.4	158±20
GS7	M	27.9±1.4	482±24	241	10.90	5.36	42.05	10.1±1.2	13.8±1.6	286±48
GS8	U	58.8±3.6	1016±61	567	11.49	1.49	43.26	21.3±4.1	22.4±4.3	220±55
UDF1	U	57.4±2.9	987±49	536	11.03	3.45	43.92	12.6±0.8	16.0±1.0	162± 18
UDF2	M	26.0±1.3	448±22	120	11.07	1.71	–	8.3±1.1	10.3±1.4	231± 42
UDF3	M	53.4±2.7	928±46	41	10.13	32.61	42.66	11.3±0.6	25.4±1.3	274± 27
UDF4	M	10.6±0.6	183±11	48	10.60	2.17	–	2.9±0.3	4.7±0.5	257± 43
UDF5	M	7.7±0.4	132± 7	127	10.39	3.67	–	4.8±0.8	8.8±1.5	669±147
UDF6	S	9.1±0.5	157± 8	–	10.71	2.88	–	4.0±0.6	6.0±0.9	383± 76
UDF7	M	11.2±0.6	194±10	95	10.49	2.93	42.68	2.5±0.2	4.4±0.3	224± 26
UDF8	S	9.9±0.5	173± 9	154	11.12	1.49	43.70	3.2±0.5	3.9±0.6	227± 44
UDF11	M	22.5±1.1	396±19	267	10.80	3.99	42.38	4.8±0.2	6.9±0.3	173± 17
UDF13	S	7.4±0.5	128± 9	166	10.81	0.96	42.45	1.9±0.3	2.7±0.4	214± 46
UDF16	S	3.2±0.2	54± 3	–	10.80	1.01	–	1.7±0.5	2.4±0.7	439±145

Notes: Col.(1) Simplified ID. Col.(2) Visual morphological classification of the rest-frame optical images of the galaxies (from *HST*-WFC3 *H*-band): single/isolated galaxy (S), merger (M) and undefined (U). Col.(3) Total IR ($8 - 1000 \mu m$) luminosity measured from the fit of the data from *Spitzer*, *Herschel* and ALMA. Col.(4) Total SFR=SFR$_{IR}$+SFR$_{UV}$ in $M_\odot$.yr^{-1} where both SFR are defined in Eq. 5 and Eq. 6. Col.(5) SFR derived from the fit of the UV-optical-near IR SED in $M_\odot$.yr^{-1} assuming a contant SFR history. Col.(6) Logarithm of the stellar mass (Salpeter IMF). Col.(7) Starburstiness, R_{SB}=SFR/SFR$_{MS}$, where SFR$_{MS}$ is the MS SFR at the redshift of the galaxy. Col.(8) Logarithm of the total 0.5–8 *keV* X-ray luminosities in erg.s^{-1} from Luo et al. (2017). Col.(9) Dust mass derived from the fit of the far-IR SED (see Sect. 2.4). Col.(10) Gas mass derived from the dust mass in Col.(10) following the recipe for the dust-to-gas ratio described in Sect. 2.4. Col.(11) Depletion time, τ_{dep} (=M$_{gas}$/SFR), in Myr.

in Table 3 together with the total IR luminosities obtained from the SED fitting described in Section 2.4.

The positions of the ALMA galaxies in the SFR–M$_\star$ plane are shown in Fig.5 where the eight galaxies from our GOODS-*South* observations are marked with green filled circles. The dashed and two solid black lines show the median and its 68 % standard deviation determined by Schreiber et al. (2015). The full catalog of GOODS-*South* galaxies at 1.5<z<2.6 is presented with orange and blue dots for the galaxies with and without an *Herschel* detection respectively. For the galaxies with no *Herschel* detection, we used SFR$_{SED}$ (blue dots) while for galaxies with an *Herschel* detection, we used SFR$_{tot}$ (orange dots). Because of the large redshift range used here to select the z∼2 galaxies (1.5<z<2.6), we have corrected the SFR of each galaxy for the evolution of the MS between its redshift and z=2. As a result, the SFR of a galaxy located at a redshift z=1.6 is shown on Fig.5 with a higher SFR value equal to its actual SFR multiplied by a factor SFR$_{MS}^{z=2}$/SFR$_{MS}^{z=1.6}$. This normalization factor facilitates the presentation of the location of the ALMA targets relative to the MS.

In the following, we will use a single parameter to quantify this distance to the MS called the "starburstiness" as in Elbaz et al. (2011), i.e., R_{SB}=SFR/SFR$_{MS}$. Out of the present list of ALMA targets, only 15 % (or 31 %) may be considered as "starbursts" defined as galaxies with a starburstiness R_{SB}>4 (or >3; see Table 3). The remaining 85 % (or 69 %) consist of galaxies located in the upper part of the MS or slightly above the 68 % *rms* of 0.3 dex of the MS. In the following, we will call "MS galaxy" a galaxy located within one standard deviation of the

MS SFR and use the starburstiness to quantify the distance to the MS rather than employ a bimodal separation.

3. Results

3.1. Serendipitous detection of an "HST–dark" galaxy at z∼3

In one out of the 8 GS galaxies, GS8, we found an offset between the ALMA and *H*-band centroids that we attribute to a projection effect, the ALMA source being associated to a background source. The red part of Fig. 6-right showing the *H*-band contribution to the *VIH* image shows a clear extension to the North. The offset of 0.35″between the UV and ALMA centroids is similar to those observed for some of the other galaxies studied here. However, there are three reasons why we believe that the ALMA emission is associated to another galaxy in the case of GS8.

First, there is this offset of 0.35″between the *H*-band and the ALMA centroids, and not only with the UV. Second, the photometric redshift of the foreground galaxy associated with the UV image is z_{phot}=1.101 whereas the far-infrared SED combining the *Herschel* and ALMA photometric points peaks at $350 \mu m$. If the far-IR emission were associated with this galaxy, it would peak at a rest-frame λ= 167 μm as opposed to the typical galaxies at this redshift which peak around λ= 100 μm. Third, this galaxy (CANDELS ID = 5893) has an estimated stellar mass of M$_\star$=4.6×10^9 M$_\odot$. At a z_{phot}=1.101, this galaxy would have an extreme starburstiness of R$_{SB}$=60 and if the whole far-IR emission was to be attributed to this galaxy, it would lead to a dust mass of M$_{dust}$=7.9×10^9 M$_\odot$, i.e., 1.7×M$_\star$, and a gas mass of M$_{gas}$=2.5×10^{12} M$_\odot$. Considering these unrealistic dust
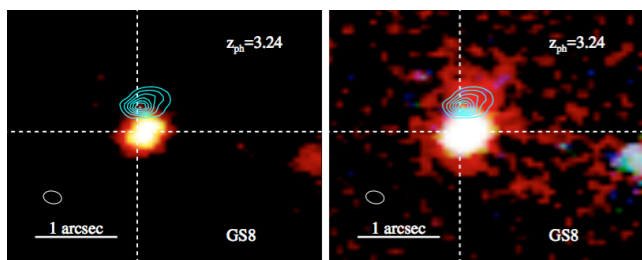
Fig. 6. ALMA contours overlaid on *HST* images of the galaxy GS8. The rest-frame UV light distribution is presented alone on the ***left*** (combination of the *HST*–ACS F606W and F814W bands). The RGB image on the ***right*** includes as well the *HST*–WFC3 F160W band (1.6 μm) sampling the rest-frame *V*-band.

temperatures and masses, together with the spatial distribution of the ALMA and *H*-band light, we believe that the *Herschel* and ALMA emission arise primarily from a background galaxy. Since the foreground galaxy has the CANDELS ID 5893, we decided to call the background galaxy 5893b.
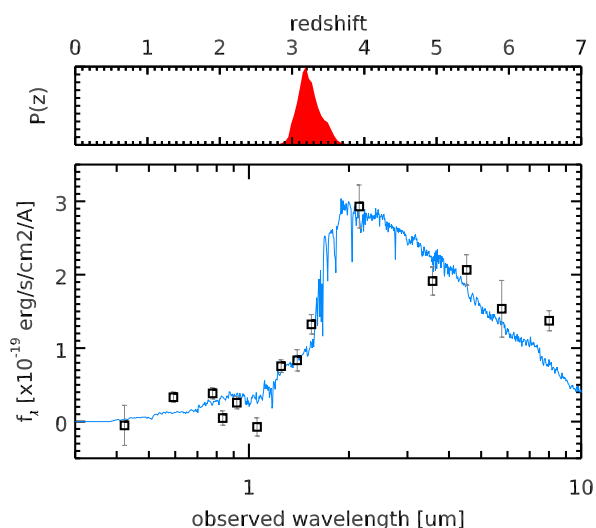
Fig. 7. Spectral energy distribution of the offset source GS8 (5893b) measured from aperture photometry at the location of the ALMA source. The photometric redshift probability distribution peaks at z=3.24.

In order to determine the photometric redshift of this galaxy, we modelled the light profile of all the other surrounding galaxies within an 8″ radius as single Sérsic profiles using `imfit` (Erwin 2015) on the HawK-I *Ks*-band image (PSF FWHM=0.4 arcsec, Fontana et al. 2014). We then used the results of this modelling to measure the photometry on all the *HST* images from F435W to F160W, as well as in the *Spitzer* IRAC images from 3.6 to 8 μm. We convolved the Sérsic profiles with the point-spread function of the corresponding image, and only varied the total flux of each galaxy to minimise the χ^2 of the residuals. The resulting photometric measurements for ID5893b are shown in Fig. 7. After this process, ID5893b was only clearly detected in bands *J*, *H* from *HST*–WFC3, *Ks* from HawK-I, and all the *Spitzer* IRAC bands where it clearly dominates over ID5893.

The photometry obtained for GS8 (ID5893b) was then used to determine a photometric redshift with the program EAZY and a stellar mass with the program FAST. We found z_{phot}=3.24±0.20 and $M_\star$=3× 10^{11} $M_\odot$. This photometric red-
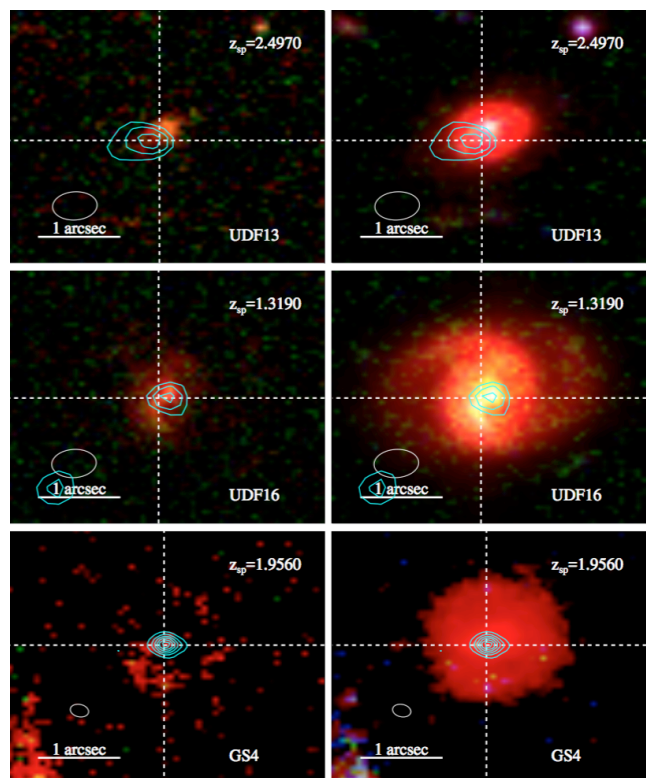

Fig. 8. ALMA contours on *HST* images for main sequence galaxies. ***Left*** column: rest-frame UV from ACS F606W & F814W, i.e., 2020 & 2710 Å at z~2. ***Right*** column: R,G,B=5300,2700,2000 Å from ACS bands F606W and F814W and WFC3 band F160W at z~2. The ALMA contours correspond to 1.3mm for the UDF sources and 870 μm for the GS source.

shift is consistent with the observed peak of the far-IR SED of ID5893b located at λ_{peak}~ 350 μm.

The resulting starburstiness of GS8, R_{SB}=1.49, corresponds to a typical MS galaxy at z~3.24. The fit of the far-IR SED using the Draine & Li model gives a dust mass of M_{dust}=2.3×10^9 $M_\odot$, which is lower than the value estimated for the z=1.101 redshift because the dust mass is very sensitive to the dust temperature, which is much higher here since the peak emission is now located close to 85 μm. The gas fraction, f_{gas}=M_{gas}/(M_{gas}+$M_\star$), is also reasonable (as opposed to the low redshift option) since it now reaches a value of 40 %.

To conclude, ALMA allowed us to identify a distant counterpart to a previously detected *Herschel* source that was not present in the CANDELS *HST* catalog (Guo et al. 2013). If one considers the *H*-band extension that we analyzed above, then GS8 is not strictly speaking an *HST*-dark galaxy, but without ALMA it would have remained *HST*-dark. We can only extrapolate the implications of this finding on the GS sample of 8 galaxies because the UDF galaxies were selected in a blank field that would require an analysis of the existence of *HST*-dark sources over the whole field. Extrapolating from our small sample, one may expect 10-15 % of the ALMA detections to be associated with an optically dark galaxy. This statement will be studied on a firmer statistical ground in a forthcoming paper discussing a 6.7 ×10 arcmin^2 extragalactic survey in GOODS-*South* with ALMA at 1.1mm (PI D.Elbaz, Franco et al. in prep.).
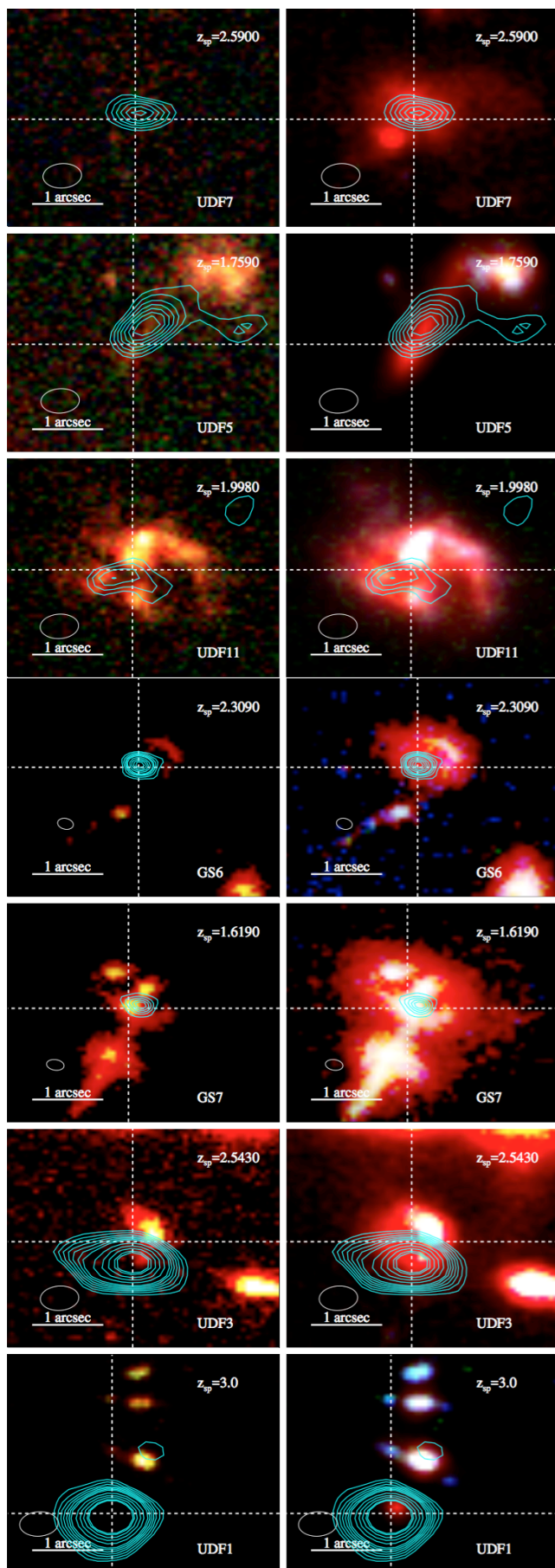
Fig. 9. Same as Fig. 8 for the "starburst" galaxies with $R_{SB}>3$ sorted by increasing R_{SB} from top to bottom.

3.2. Compact star-formation in $z\sim2$ galaxies

The ALMA images probe the dust continuum emission at typical rest-frame wavelengths of λ^{rest}_{GS}=260 μm (870 μm observed from $\bar{z}_{GS}$=2.3) and λ^{rest}_{UDF}=380 μm (1.3mm observed from $\bar{z}_{UDF}$=2.43) for the GS and UDF galaxies respectively. We will consider that these two wavelengths are close enough to probe the same physical origin. We will assume that the median 325 μm wavelength for the whole sample probes the location of the dust heated by the newly formed young stars and that it can therefore be used to trace the geometry of the star-formation regions.

We show in Fig. 8 the example of three MS galaxies with the optical morphologies of face-on disks. Fig. 9 presents the images of the "starbursts" of our sample, defined here as galaxies with a starburstiness of R_{SB}>3.

The first remarkable result that comes out of the resolved dusty star-formation maps obtained with the high angular resolution mode of ALMA is their compactness. The optical sizes measured by van der Wel et al. (2012) using a Sérsic profile fitting of the *HST-H* band images are compared to the ALMA sizes, computed using 2D Gaussian profiles, in Fig. 10. Both are circularized as in Eq. 1. As discussed in Section 2.3.2, the Gaussian and Sérsic fits to the ALMA data provide similar sizes.

Over the whole sample of 19 $z\sim2$ star-forming galaxies resolved with ALMA, we find that the ALMA sizes are systematically smaller than the rest-frame *V*-band sizes. Similar results have been systematically found by several different authors using galaxy samples selected with different strategies (e.g., Hodge et al. 2016, Barro et al. 2016, Rujopakarn et al. 2016, Fujimoto et al. 2017). Using a compilation of ALMA observations with typical angular resolutions of ~0.6 arcsec (as compared to 0.2 arcsec here), Fujimoto et al. (2017) measured a factor of $R^{circ}_H/R^{circ}_{ALMA}\sim$1.4 (see their Fig.12) that we have represented with a dashed line in Fig. 10. We can see that most of our galaxies fall within a factor two around this ratio (dotted lines in Fig. 10) except a sub-population of compact sources that we will discuss in more detail in the following.

We note however an important caveat related to our sample selection. The condition that we imposed on our targets resulted in selecting exclusively massive star-forming galaxies with a median $M_\star\sim$1.4$\times10^{11}$ $M_\odot$. If massive galaxies turned out to exhibit particularly compact star-formation distributions, they may not be the most representative objects to study the impact of giant clumps of star-formation. As we will show in the next sections, massive galaxies do turn out to exhibit particularly compact star-formation as also found by Barro et al. (2016) and as one would expect if they were candidate progenitors of the population of compact ellipticals at $z\sim2$ (van der Wel et al. 2014).

As discussed in Section 2.3.2 (see also Rujopakarn et al. 2016), the S/N ratio on the UDF ALMA sources in not high-enough to provide a robust Sérsic profile fitting and derive a Sérsic index. But for the higher-quality of the GS galaxies, we find that the ALMA profiles can be fitted by a Sérsic profile with a median Sérsic index is n=1.27±0.48, hence close to an exponential disk. The dusty star formation regions therefore seem to be disk-like, confirming what was previously found by Hodge et al. (2016).

3.3. An ALMA view on kpc clumps of star formation

The discovery of giant star-forming regions in the high-redshift population of so-called "chain galaxies" and "clump-cluster galaxies" revealed by the first generation of deep *HST* images (Cowie et al. 1995, Elmegreen & Elmegreen 2005) started a still-
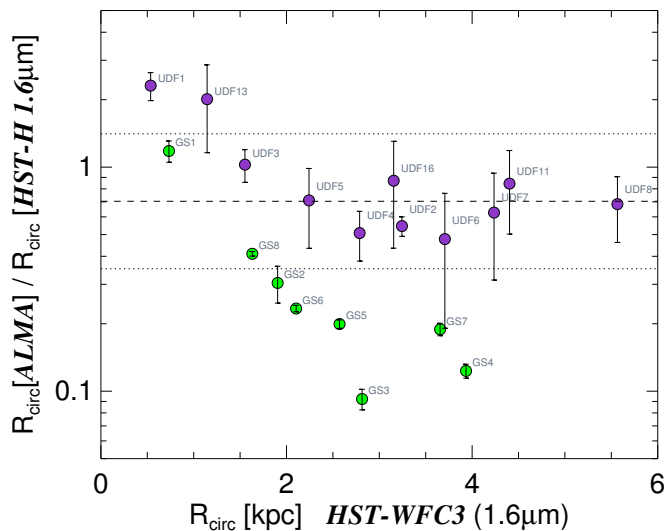
Fig. 10. ALMA circularized effective radii as a function of HST–WFC3 *H*-band effective radii from van der Wel et al. (2012).
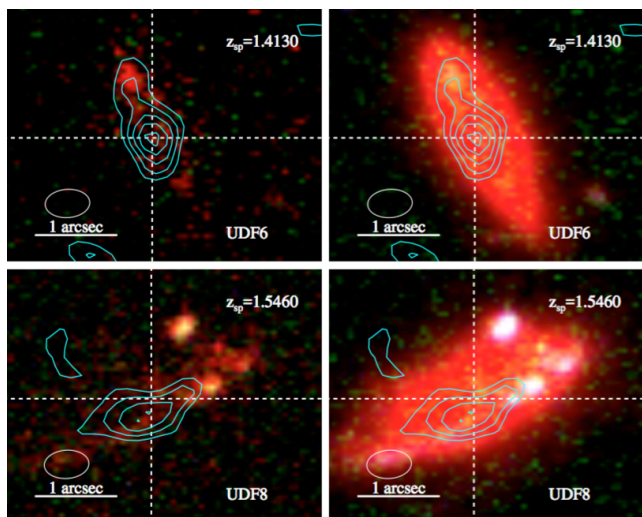
Fig. 11. ALMA contours overlaid on *HST* images of UDF6 (R_{SB}=2.9) and UDF8 (R_{SB}=1.5). Both galaxies have spectroscopic redshifts close to z~1.5, and are located in (UDF8) or close (UDF6) to the MS. The ALMA contours show the light distribution of the observed 1.3mm wavelength corresponding to 520 μm in the galaxies rest-frame. The 1 arcsec line corresponds to 8.5 kpc at z=1.5. The Northern giant UV clump of UDF6 and the three clumps of UDF8 (on the N-W side of the galaxy) have a size of 0.25″ corresponding to proper sizes of 2 kpc. The ALMA contours start from 80 μJy and increase with steps of 20 μJy.

ongoing debate on their role in the stellar mass growth and morphological transformation of galaxies throughout cosmic time. Expected to form as a result of dynamical instabilities in high-redshift gas-rich galaxies, those kpc-size ~10^8 $M_\odot$ clumps of star formation could lead to the formation of the central bulge of galaxies if they lived long enough to survive their migration from the peripheries to the centers of galaxies (Elmegreen et al. 2008).

How much of the integrated stellar mass growth of a galaxy comes from these kpc clumps remains uncertain. Since z~2 galaxies with strong SFR systematically radiate most of their energy from star formation in the far-infrared/submm, it is only by resolving these galaxies at these long wavelengths that one will be able to determine the role of kpc-clumps. If kpc-large

clumps of star formation were responsible for a large fraction of the resolved far-IR emission of galaxies, this would imply that the physical mechanism responsible for their formation plays an important role in shaping present-day galaxies.

In a recent paper, Hodge et al. (2016) studied the possible existence of kpc-clumps of star formation with an ALMA follow-up of a sample of 16 z~2.5 SMGs with $S_{870\mu m}$=3.4–9 mJy and L_{IR}~4×10^{12} $L_\odot$. They searched for point-like sources that could be associated with kpc-clumps using a synthesized beam of 0.17″×0.15″FWHM, corresponding to a physical size of 1.3 kpc at the median redshift of z~2.5 (the analysis was also performed at a resolution of 0.12″corresponding to 1 kpc). While marginal evidence was found for residual emission that could be associated to the kpc clumps, the authors generated some simulated ALMA images of mock galaxies with smooth profiles without any clumps and found that the analysis of the resulting mock ALMA images showed similar signatures of kpc clumps with low significance. Hence they concluded that "while there may be a hint of clump-like dust emission in the current 870 μm data on kiloparsec scales, higher signal-to-noise observations at higher spatial resolution are required to confirm whether these clumpy structures are indeed real".

Cibinel et al. (2017) used ALMA to spatially resolve the CO(5–4) transition – which probes dense star formation – in the z=1.57 clumpy galaxy UDF6462. In this galaxy, the UV clumps make individually between 10 and 40 % of the total UV SFR. Using the observed $L'_{CO(5-4)}$–L_{IR} correlation (Daddi et al. 2015), they find that none of the six clumps produces more than 10 % of the dusty SFR (upper limit of ~5 $M_\odot yr^{-1}$for a total SFR =56 $M_\odot yr^{-1}$). The limit goes down to less than 18 % for the combined contribution of the clumps after stacking all 6 clumps. If this conclusion may be generalised, it would imply that the giant clumps observed in the UV are not major contributors to the bulk of the stellar mass growth of z~2 galaxies.

We designed our ALMA exposures for the 8 "GS" sources (see Section 2.3.1) to detect individual clumps of star formation at 870 μm assuming that a clump could be responsible for 20 % of the total SFR of a galaxy. In all 8 galaxies, we find that the ALMA continuum emission is concentrated in a nuclear region, with no evidence for external clump contributions, similarly to what was found by Cibinel et al. (2017) and Hodge et al. (2016).

Three galaxies among the closest sources of the UDF sample – UDF6, UDF8 and UDF16 at z_{spec}=1.413, 1.546, 1.319 respectively – present the shape of grand design spirals with a total extent in the rest-frame 6400 Å of ~20–30 kpc (observed WFC3 *H*-band in red in Fig. 11–right). UDF6 and UDF8 present clear kpc-size clumps in the rest-frame UV light distribution shown on the left panels of Fig. 11. UDF16 is a face-on spiral that will be discussed as a part of the rest of the sample since it shows no evidence for kpc size UV clumps outside its central UV nucleus.

UDF8 presents three clumps in the N-W side and UDF6 one clump in the N-E side. All four UV clumps have a total extent of 0.25″, i.e., 2 kpc at z~1.5, hence a radius of about 1 kpc. We note that both galaxies are close to the median SFR of the MS with a starburstiness of R_{SB}=1.5 and 2.9 respectively and experience a similar SFR~150 $M_\odot$ yr^{-1}. UDF8 presents the largest number of UV clumps, it is the closest galaxy to the median SFR of the MS.

At the typical redshift of z~1.5 of these galaxies, the ALMA images of the UDF at 1.3mm probe the rest-frame 520 μm emission in the rest-frame. This emission is found to peak on the center of the WFC3-*H* band images in both galaxies (crosses in Fig. 11) whereas the UV clumps present a systematic offset.
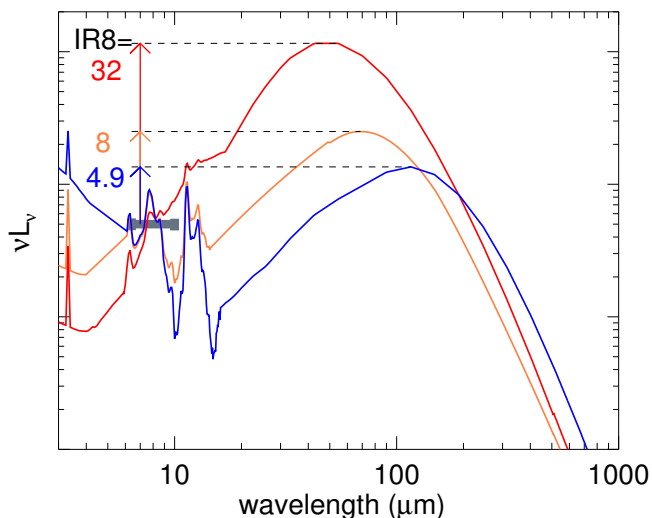
Fig. 12. Three SEDs from the Chary & Elbaz (2001) library normalized to the same $L_{8\mu m}$ (using the IRAC passband centered on $8\,\mu m$). We present the SEDs 11, 58 and 95 for which $IR8 = L_{IR}/L_{8\mu m} = 4.9$, 8 and 32 respectively. The horizontal black solid segment shows the width of the IRAC2 channel centered on $8\,\mu m$.

This offset is much larger than the astrometric uncertainty (note the perfect agreement between ALMA and *HST*) and than the ALMA PSF FWHM (ellipse on the lower-left corner). It implies that there is a clear dichotomy in these two galaxies between the young massive stars inhabiting highly attenuated dust clouds and those responsible for the bulk of the UV light. The left column of Fig. 11 shows that no UV light is detected at the location of the peak ALMA emission, which implies that the UV-slope is not a good proxy for the amount of dust extinction here.

In both galaxies, the ALMA contours do present an extension suggesting some marginal contribution of the kpc clumps to the far-infrared emission. The rest-frame $520\,\mu m$ contours of UDF6 present a second, less pronounced, peak centered on one of the kpc clump and the same is seen, slightly less pronounced, in UDF8 with a contribution from the southern kpc clump. However due to the low S/N of the 1.3mm images of these sources, this evidence is provided only by the first and second ALMA contours at the 80 and $100\,\mu Jy$ levels, i.e., only at the $2-\sigma$ confidence level. As shown by the simulations of Hodge et al. (2016) discussed above, deeper ALMA integrations would be needed to confirm the detection of the giant clumps in the far-infrared.

Assuming that the dusty star-formation is indeed not spread in a series of clumps, then we will consider that it is well characterized by its IR luminosity surface density, Σ_{IR} (Eq. 2).

3.4. Star formation compactness and IR8 color index

The IR luminosity density, Σ_{IR} – a proxy for the dusty SFR density – has been found to correlate with an integrated property of local $z \sim 0$ galaxies, the $IR8$ color index (see Fig.13 of Elbaz et al. 2011). Compact star-forming galaxies were found to exhibit large values of the $IR8 = L_{IR}/L_{8\mu m}$ color index whereas galaxies with extended star-formation presented a "normal, universal" $IR8$ ratio of $IR8 \sim 4.9$. Compact and extended star-forming galaxies were distinguished as galaxies with Σ_{IR} above and below a critical density of $\Sigma_{IR}^{crit} = 3 \times 10^{10}\ L_\odot\ kpc^{-2}$ respectively. In this Section, we present a revised version of the local $IR8 - \Sigma_{IR}$ relation and discuss its application to the distant Universe.

The $IR8$ color index measures the ratio of the continuum emission – as measured by the total mid to far-IR luminosity L_{IR}, dominantly due to the emission of big dust grains with a peak emission around $100\,\mu m$ – over the emission due to the combination of continuum emission from very small grains (VSGs) of dust and broadband features commonly attributed to polycyclic aromatic hydrocarbons (PAHs; Leger & Puget 1984, Allamandola et al. 1985) – as measured by the $8\,\mu m$ *Spitzer*-IRAC broadband filter.

In local galaxies, strong $IR8$ values (red curve in Fig. 12) are systematically associated with compact star formation taking place in merger-driven starbursts. Instead, normal spiral galaxies exhibit strong PAH equivalent widths and a weaker contribution of warm and cold dust continuum in the mid-IR and far-IR (blue curve in Fig. 12). The three template IR SEDs presented in Fig. 12 come from the Chary & Elbaz (2001) library and present $IR8$ values of 4.9, 8 and 32 respectively. Therefore in local galaxies, $IR8$ not only correlates with star-formation compactness, as probed by Σ_{IR}, but also with starburstiness, R_{SB} (see Fig.17 in Elbaz et al. 2011).

In the following, we discuss the physical origin of the $IR8 - \Sigma_{IR}$ relation that may apply to both local and distant galaxies. The interest of this relation is twofold. On one hand, it provides an empirical method to connect integrated and resolved galaxy properties that may be used to derive one from the other. On the other hand, if the relation holds in distant galaxies, $IR8$ and Σ_{IR} may both be used to separate compact and extended star formation, and may therefore serve to unveil the role of mergers.

3.4.1. Revised version of the local $IR8 - \Sigma_{IR}$ relation and discussion of its physical origin

To produce their local $IR8 - \Sigma_{IR}$ relation, Elbaz et al. (2011) used IR sizes for local galaxies coming from a combination of radio data (converted to FIR sizes using a correlation observed between FIR and radio sizes) and mid-IR sizes from *Spitzer*-IRS (from Díaz-Santos et al. 2010).

Here we use sizes directly measured in the far-IR coming from an *Herschel*-PACS $70\,\mu m$ follow-up of local LIRGs from the Great Observatories All-sky LIRG Survey (GOALS; Armus et al. 2009). Sizes were measured for a total 293 galaxies including 42 normal galaxies ($10 \leq \log(L_{IR}/L_\odot) < 11$), 175 LIRGs ($11 \leq \log(L_{IR}/L_\odot) < 12$) and 22 ULIRGs ($12 \leq \log(L_{IR}/L_\odot)$). The sizes measured for these galaxies (as described in Díaz-Santos et al. 2017) were used to produce the revised version of the local $IR8 - \Sigma_{IR}$ relation presented in Fig. 13-top. We also included 11 galaxies with radio sizes (filled squares) and 39 galaxies with mid-IR sizes from AKARI (filled stars) that were originally used in Elbaz et al. (2011).

This revised $IR8 - \Sigma_{IR}$ relation for local galaxies is amazingly tight with a 68 % median absolute deviation (MAD) of only 0.11 *dex*. The polynomial fit to the sliding median (Eq. 7) and its MAD are represented by the solid and dashed lines in Fig. 13.

$$\log_{10}(IR8) = (1.02 \pm 0.11) + 0.37 \times \log_{10}\left(\Sigma_{IR}/10^{11}\right) + 0.08 \times \left[\log_{10}\left(\Sigma_{IR}/10^{11}\right)\right]^2 \tag{7}$$

We find that the trend is relatively flat up to $\Sigma_{IR}^{crit} \sim 3 \times 10^{10}$ $L_\odot\ kpc^{-2}$ and then rises steeply. Although continuous, this improved relation confirms the existence of two regimes of star formation. Galaxies with extended star formation ($\Sigma_{IR} < 3 \times 10^{10}\ L_\odot$ kpc^{-2}) have $IR8 = 4-5$, whereas compact star-forming galaxies reach $IR8$ values well above 10.
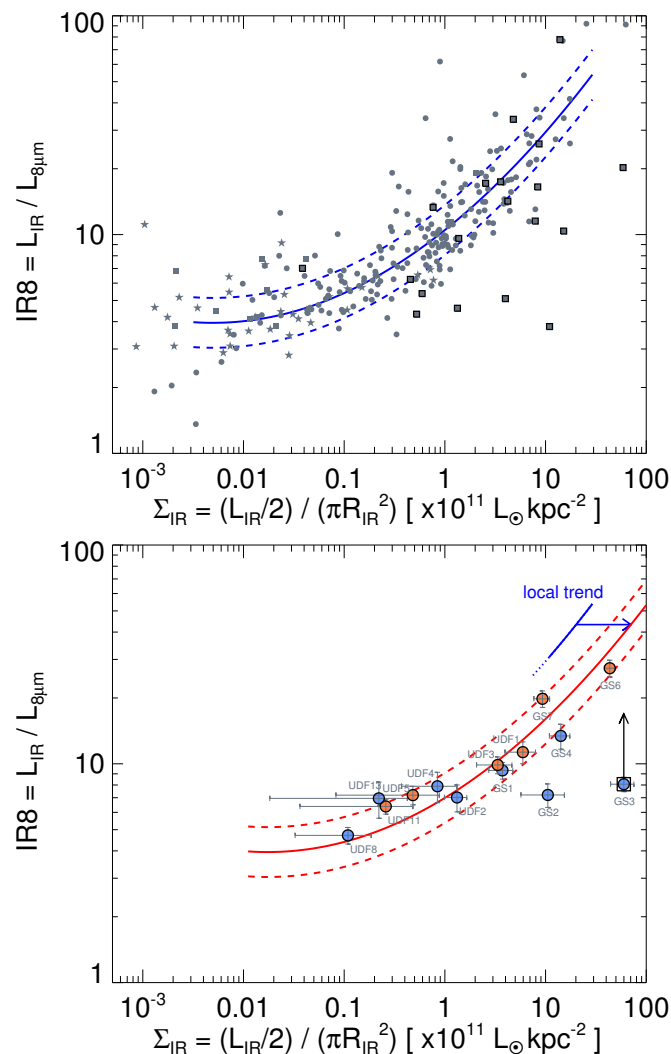
Fig. 13. *Top: IR*$8 - \Sigma_{IR}$ relation for local galaxies. Grey filled dots: 293 galaxies with *Herschel* PACS 70 μm sizes ($R_{IR}=R_{70\mu m}$) from Díaz-Santos et al. (2017). Filled squares and stars: 11 and 39 galaxies with radio and mid-IR sizes from Elbaz et al. (2011). Galaxies with mid-IR spectral signatures of AGNs (identified by Díaz-Santos et al. 2017) are marked with bold squares. The solid blue line is a polynomial fit to the sliding median described by Eq. 7. The two dashed lines 30 % above and below (± 0.11 *dex*) encompass 68 % of the galaxies. *Bottom:* position of the $z{\sim}2$ ALMA sources on the *IR*$8 - \Sigma_{IR}$ diagram. The solid and dashed red lines show the local relation shifted to the right by a factor 3.5 to account for the combined effects of the rise of the MS SFR with redshift and decrease of galaxy sizes with redshift. Blue and orange filled dots separate galaxies on or close to the MS ($R_{SB}\leq 3$) from starbursts ($R_{SB}>3$). Only galaxies within $1.5\leq z\leq 2.5$ are shown here because the determination of L_8 from the observed 24 μm flux density would require a a large and uncertain extrapolation. The black square on GS3 indicates that it is a power-law for which the contribution of the AGN has been corrected in a conservative way.

We wish to emphasize that most of the outliers below the relation are galaxies identified as power-law AGNs by Díaz-Santos et al. (2017) from their mid-IR spectra (thick black squares in Fig. 13-top). This trend may either be explained by *(i)* a contribution to the 8 μm emission by warm dust heated by AGN, and/or *(ii)* a physical connection between star-formation compactness and AGN activity.

The physical origin of this tight correlation can now be better understood thanks to the analysis of Díaz-Santos et al. (2017)

who present a similarly tight relation between $L_{IR}/L_{[CII]158\mu m}$ and Σ_{IR}. The [CII]158 μm emission comes from the same region as the PAHs that participate to the 8 μm luminosity, namely the PDR or photo-dissociation region. In both cases, there is a nearly flat *IR*8 and $L_{IR}/L_{[CII]158\mu m}$ ratio with increasing Σ_{IR} up to the same critical density, $\Sigma_{IR}^{crit} \sim 3\text{--}5\times 10^{10}$ L$_\odot$ kpc^{-2} (see their Fig.2-middle right, which shows $L_{[CII]158\mu m}/L_{IR}$ analog to $1/IR8$ here). Then *IR*8 and the $L_{IR}/L_{[CII]158\mu m}$ ratio both increase with increasing Σ_{IR}. This behavior may be understood with the concept of "dust-bounded" star-formation nebulae described in Abel et al. (2009). The idea proposed in this paper and discussed in Díaz-Santos et al. (2017) involves the role of dust that absorbs part of the ionizing radiation and therefore prevents it from reaching the PDR region. This leads to a rise of the dust temperature and consequently also of the total IR luminosity emitted, proportional to $T_{dust}^{4+\beta}$ (where β is the emissivity of the dust), and a drop of the emission in [CII] and PAHs from the PDR. In the local Universe, merger-driven starbursts are systematically associated with such young and compact star-formation regions that may be considered as dust-bounded, with the consequence that *IR*8 and $L_{IR}/L_{[CII]158\mu m}$ rise during the merger-driven starburst. Díaz-Santos et al. (2017) find that the ratio of the intensity of the interstellar radiation field, G, over the average PDR hydrogen density, n_H, G/n_H, remains constant below Σ_{IR}^{crit} and increases rapidly with Σ_{IR} above Σ_{IR}^{crit}.

3.4.2. The *IR*$8 - \Sigma_{IR}$ relation for $z{\sim}2$ ALMA galaxies

The positions of the $z{\sim}2$ ALMA galaxies in the *IR*$8 - \Sigma_{IR}$ plan are shown in Fig. 13-bottom. *IR*8 values were only be computed for galaxies with $1.5\leq z\leq 2.5$ in order to include the dominant 7.7 μm PAH feature in the observed *Spitzer*-MIPS 24 μm passband. The power-law AGN GS3 (see Fig. 4, GS5 and GS8 are out of the redshift range where *IR*8 can be computed) is marked with a bold square and an upper arrow. This arrow illustrates the fact that the AGN contribution to the rest-frame 8 μm luminosity is uncertain. Our estimate of L_8 was done assuming a conservative SED for the star-formation component. This assumption does not affect the determination of L_{IR} but does affect L_8. We found that using an SED like Arp 220, for example, would nearly equally well fit the IR SED if the AGN produced the bulk of L_8. In this case, *IR*8 would be increased by a large factor, potentially bringing the galaxy in the relation followed by the rest of the sample.

First, we note that the $z{\sim}2$ samples follows a correlation like the local galaxies. Second, one can see that galaxies *on* and *above* the MS are not separated as it is the case for local galaxies where "starbursts" present a compact geometry with $\Sigma_{IR}^{crit}>\Sigma_{IR}^{crit}$ while MS galaxies experience more extended star-formation. Galaxies three times above the MS (i.e., with $R_{SB}>3$) are marked with orange symbols in Fig. 13-bottom, while MS galaxies below this R_{SB} value are represented with blue symbols. Both types span the full dynamic range in Σ_{IR}. However, as we will see in the following, it is possible that some of our MS are actually experiencing a merger that enhances their star-formation by a moderate factor.

In the framework of the dust-bounded star-formation regions interpretation that we discussed above, galaxies with a larger *IR*8 are observed in a younger stage, that precedes the destruction of the dust within the HII region. However, the typical Σ_{IR} of a galaxy at the median redshift of $z{\sim}2.3$ of our sample was larger than that of a local galaxy. We estimate this factor to be around ~ 3.5 as a result of the fact that the SFR of MS galaxies was 20

times greater (Schreiber et al. 2015) and the typical size of a star-forming galaxy was $(1+z)^{0.75}$ times smaller (van der Wel et al. 2012). We find that the red solid and dashed lines that represent the local $IR8 - \Sigma_{IR}$ relation shifted by this factor 3.5 do provide a good fit to the ALMA data. This suggests that $IR8$ may serve as a good proxy for Σ_{IR} even in the distant Universe.

We note that high-redshift galaxies being more metal-poor than galaxies today, this could also play a role in reducing PAH emission and increasing $IR8$ at higher redshifts, as discussed in Shivaei et al. (2017). However, star-formation in high-z galaxies is taking place both in more compact regions and in less metal-rich environments, and disentangling both effects might be quite complex (see Schreiber et al. 2017).

3.5. Star formation compactness and AGN activity

Out of our sample of 19 ALMA galaxies, 11 are detected in X-rays with the 7 Msec exposure of the *Chandra* Deep Field-*South* image (Luo et al. 2017). Following the commonly used AGN definition (also used in Luo et al. (2017)), we classify an X-ray source as an AGN when its total X-ray luminosity integrated over the whole $0.5 - 7$ keV range satisfies $L_X \geq 10^{42.5}$ erg s^{-1}. With this AGN definition, we detect a total of 8 AGNs. The three power-law AGNs (see Fig. 4) are all identified as X-ray AGNs with $L_X \geq 10^{43}$ erg s^{-1}.

We find that the proportion of galaxies hosting an AGNs rises with increasing Σ_{IR}: 75 % of the galaxies with $\Sigma_{IR} \geq 3 \times 10^{11}$ L$_\odot$ kpc^{-2} harbor an AGN (6 out of 8 galaxies). Hence there is a clear increase of the fraction of AGNs among the galaxies with compact star-formation within the limited statistics of the present sample. This suggests that the physical mechanism responsible for the rise in star-formation compactness also efficiently feeds the central black hole. Such a relationship was also found by Chang et al. (2017).

We also note that only 25 % of the AGNs are associated with galaxies the we visually classified as morphologically disturbed, i.e., mergers. The rest of the AGN population is morphologically classified as either isolated or unknown. Interestingly, the AGN fraction exhibits a tighter link with the FIR luminosity density, hence with the star-formation compactness, than with the visual identification of a merger signature. However, we cannot rule out the possibility that these galaxies are in the late-stage of a merger, which at these redshifts would not present clearly identifiable morphological perturbations. We discuss in Section 4.3 the possibility that some of the MS galaxies may be in such a late-stage merger phase.

4. Starbursts *in* and *out* of the star-formation main sequence

4.1. Starbursts above the main sequence

Surprisingly, we do not find within our galaxy sample any clear trend between the distance to the MS, or starburstiness R_{SB}, and the depletion time (inverse of the star-formation efficiency, SFE) or with the IR luminosity surface density (see Fig. 14). Instead, we do see a trend between starburstiness and morphology.

We visually classified galaxies from the *HST H*-band images, hence in the rest-frame visible, in two broad categories: single/isolated galaxy (S), with no clear sign of perturbation, and galaxies with a perturbed morphology that we listed as mergers (M) in Table 3. Two cases are listed as undefined: GS8, discussed in detail in Section 3.1, and UDF1, which appears point-like even in the *HST* image. We note that galaxies classified as "S" may be
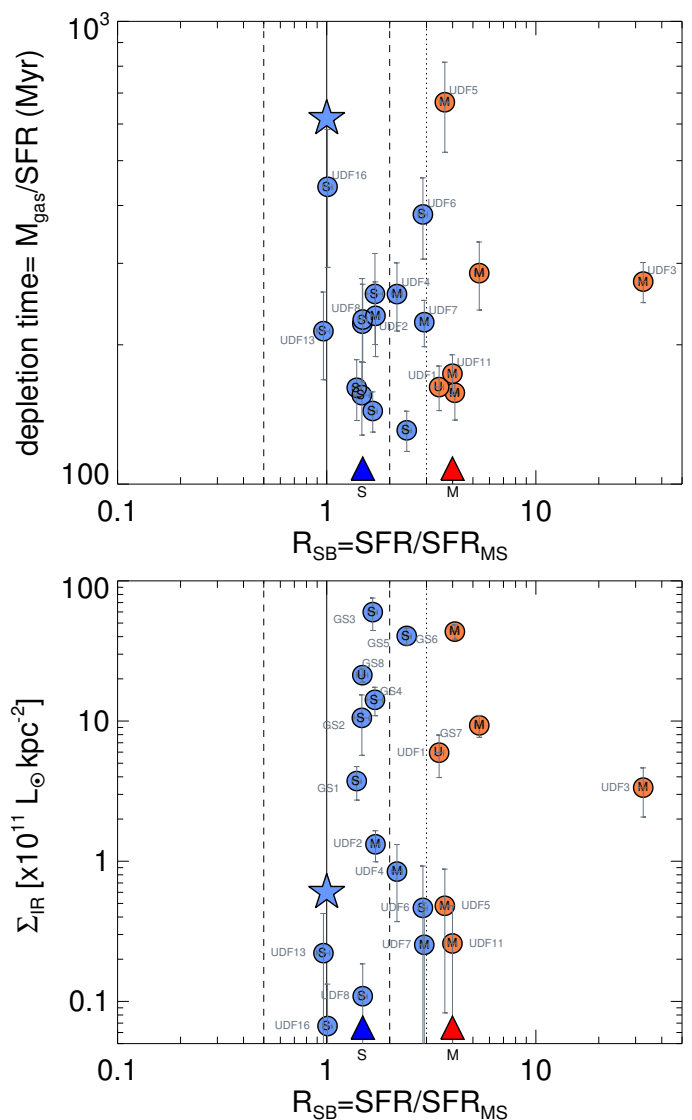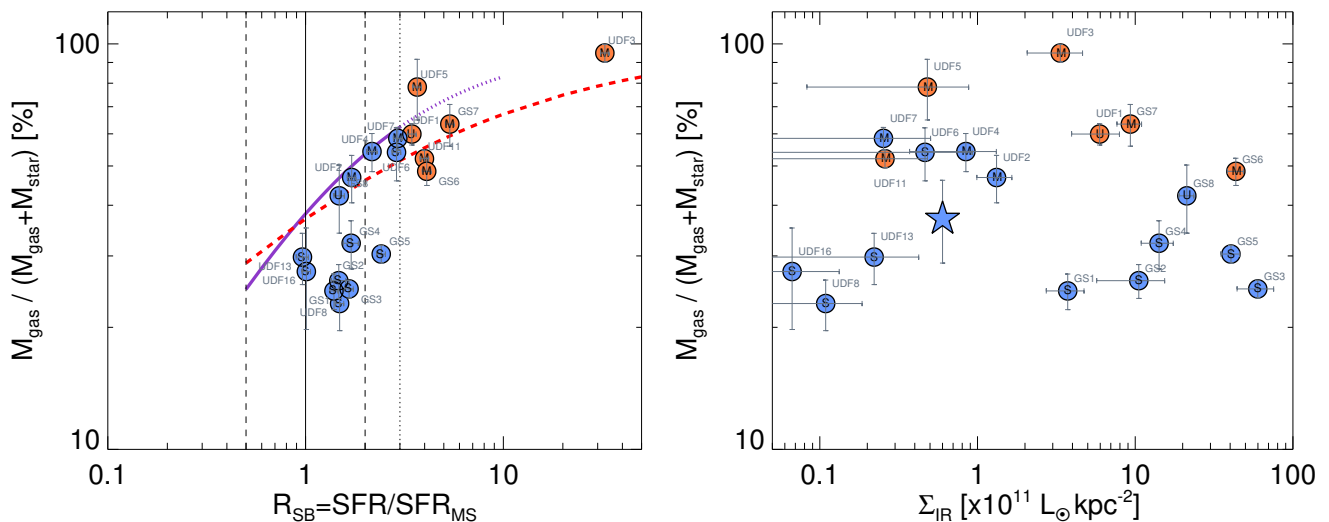
Fig. 14. Depletion time (*top*) and IR luminosity surface density, Σ_{IR} (*bottom*), as a function of starburstiness, $R_{SB} = $ SFR / SFR$_{MS}$. Blue and orange filled dots separate galaxies on or close to the MS ($R_{SB} \leq 3$) from starbursts above the MS (i.e., $R_{SB} > 3$). The letter in the symbols indicate the morphology of the galaxies from visual classification as in Table 3. The median position of mergers (M) and "single/isolated" (S) galaxies are indicated at the bottom of each plots with a red and blue triangle respectively. The blue star in the upper figure shows the typical depletion time of $z \sim 2$ MS galaxies (Tacconi et al. 2017).

late-stage mergers and we will indeed suggest so in the following for a sub-sample of the ALMA galaxies. The morphological type of the ALMA galaxies is indicated in the symbols in Fig. 14 and in the following figures of the paper.

The median starburstiness of the S-type and M-type galaxies are marked with a blue and red triangle in the bottom of both plots in Fig. 14. We can see that S galaxies are located close to the median of the MS whereas M galaxies have a typical starburstiness of $R_{SB} = 4$. This finding is consistent with the one previously found by Kartaltepe et al. (2012). The optical shapes of all the "starburst" galaxies (with $R_{SB} > 3$) are systematically very disturbed as we showed in Fig. 9, except for the point-like source UDF1.

In order to have a representative idea of the position of typical MS galaxies, we have determined the characteristic IR lu-

Fig. 15. Gas fraction (in %) as a function of starburstiness, R_{SB} (*left*, error bars in the bottom of the plot), and IR luminosity surface density, Σ_{IR} (*right*). Blue and orange filled dots separate galaxies on and 3× above the MS; the letters indicate the morphology as in Fig. 14. The dashed red line in the left figure shows the relation obtained by Tacconi et al. (2017) (see their Fig.4) converted to a Salpeter IMF: $M_{gas}=(M_\star/1.7)\times R_{SB}^{0.54}$. The solid purple line shows the relation obtained by Magdis et al. (2012a) scaled to the median stellar mass of the sample $M_\star=10^{11}$ M$_\odot$.

minosity surface density, depletion time and gas fraction of a z=2.3 galaxy of $M_\star=1.4\times10^{11}$ M$_\odot$ galaxy, the median redshift and mass of our sample that we show with a filled blue star in the figures of this paper. The SFR of a such MS galaxy is SFR^{MS}= 224 M$_\odot$ yr^{-1} (from Schreiber et al. 2015), which corresponds to L_{IR}^{MS}=1.3×10^{12} L$_\odot$ using the Kennicutt (1998) relation for a Salpeter IMF. The typical H-band size of such galaxy is given by the relation shown in the Fig.5 of Tadaki et al. (2017): $\log_{10}[R_e^{MS}(H)]$=0.14×$\log_{10}[M_\star^{Salpeter}/1.7]$-1.11, i.e., 2.6 kpc. We used the tyical $R_e^{MS}(H)/R_e^{MS}(870\mu m)$=1.4 ratio from Fujimoto et al. (2017) to derive a characteristic ALMA size of $R_e^{MS}(870\mu m)$= 1.85 kpc. The resulting characteristic IR luminosity surface density is Σ_{IR} = 6×10^{10} L$_\odot$ kpc^{-2}. We used the relations given in Tacconi et al. (2017) to derive the typical depletion time and gas fraction: τ_{dep}= 617 Myr and f_{gas}=37 % respectively, where f_{gas}=M$_{gas}$/(M$_{gas}$+M$_\star$).

We find that the gas fractions of our ALMA galaxies follow the trends found by Magdis et al. (2012a) and Tacconi et al. (2017) (Fig. 15-left) except for a sub-sample of MS galaxies with low gas fractions that will be discussed in Section 4.3. Interestingly, the starburst galaxies present the largest gas fractions while they do not exhibit the shortest depletion times. This suggests that the enhanced SFR in these galaxies is more driven by their large gas content than by their star formation efficiency. The gas fraction does not appear to change with IR luminosity surface density (Fig. 15-right). Our sample is too small to derive firm conclusions on the variation of the gas fractions with starburstiness but several studies find such an increase, although the actual amount of this rise is still debated (Genzel et al. 2015, Tacconi et al. 2017, Scoville et al. 2016). This increase of the gas fraction during a merger event could be due to the impact of the merger on the circum-galactic gas surrounding the galaxies before the merger. This gas may be driven towards the center of the galaxies. Hydrodynamical simulations accounting for the presence of circum-galactic matter, and its possible infall induced during a merger, do not exist at present to our knowledge. Such simulations should be performed to test this hypothesis.

We note a potential caveat in this analysis that is related to the metallicity of dusty starbursts. If the metallicity of starbursts
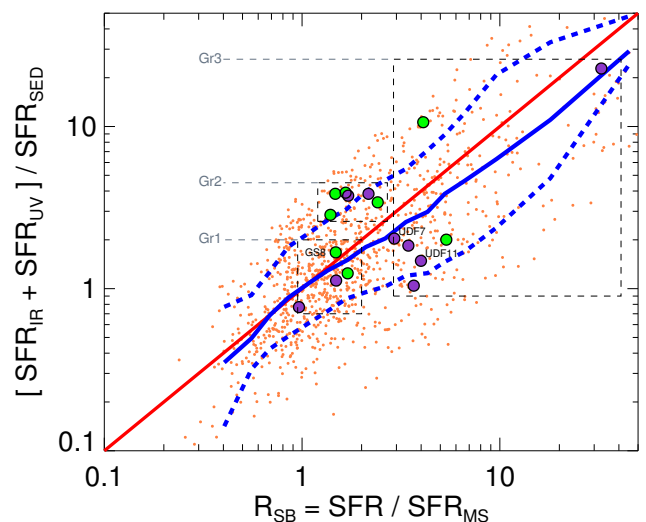
Fig. 16. Excess of total SFR, SFR$_{tot}$=SFR$_{IR}$+SFR$_{UV}$, with respect to the SFR$_{SED}$ determined by fitting the rest-frame UV-optical-NIR, as a function of starburstiness, R_{SB}=SFR$_{tot}$/SFR$_{MS}$. The orange dots show the positions of the galaxies from all four CANDELS fields with an *Herschel* detection with 1.5≤z≤2.5. Sliding median of the orange points in thick solid blue line and 68 % median absolute deviation in dashed. The green and purple symbols indicate the GS and UDF galaxies respectively.

above the MS was found to be systematically higher than the one of galaxies of similar masses within the main sequence (as suggested by Silverman et al. 2015, Puglisi et al. 2017), this would lead to an overestimate of their gas content, hence an underestimate of their star formation efficiency.

4.2. Spatial offset between UV and far-IR light distributions

We can see in Fig. 9 that there is a systematic offset between the UV and ALMA light distributions in starbursts above the main sequence. Such spatial separation was already noticed in the literature (see Rujopakarn et al. 2016, Barro et al. 2016, Hodge et al. 2016). This suggests that the use of the UV emission to

determine the total SFR of starburst galaxies may lead to strong underestimates, even when accounting for a dust attenuation correction based on the UV slope. We show that this is indeed the case in Fig. 16.

The rest-frame far-UV emission of $z\sim2$ galaxies is commonly used to derive total SFR after applying a correction for dust attenuation either from the determination of the UV-slope, β, or from the modelling of the full UV-optical SED with e.g., the Calzetti et al. (2000) attenuation law (see e.g., Meurer et al. 1999, Calzetti et al. 2000, Daddi et al. 2004, Overzier et al. 2011, Buat et al. 2012, Reddy et al. 2012, Heinis et al. 2013, Pannella et al. 2015). The average consistency for most galaxies between both ways to derive total SFR – *(1)* $SFR_{tot}=SFR_{IR}+SFR_{UV}$ and *(2)* $SFR_{tot}=SFR_{SED}$ or $SFR_{UV}^{corrected}$ – suggests that the young massive stars responsible for the UV and FIR emission are located in the same region. Alternatively, this consistency would be difficult to explain if a spatial segregation was found for most galaxies.

To address this question, we compare the ratio of both estimates of the total SFR, $[SFR_{IR}+SFR_{UV}]/SFR_{SED}$, to the distance to the MS, $R_{SB}=SFR/SFR_{MS}$ (Fig. 16).

The orange dots show the positions of all the galaxies with $1.5\leq z\leq 2.5$ detected in at least one *Herschel* band (to ensure a robust determination of L_{IR}) in all four CANDELS fields (GOODS-S, GOODS-N, UDS and CANDELS-COSMOS) and in the COSMOS 2 degree field. The sliding median (thick solid blue line, and 68 % dispersion in dashed) shows that SFR_{SED} and $[SFR_{IR}+SFR_{UV}]$ provide the same estimate of SFR_{tot} within 0.3 *dex* for MS galaxies, i.e., where $R_{SB}\sim1$. The density of the orange points at the [1,1] position is not representative of the actual number of MS galaxies because our sensitivity allows us to detect only the most massive MS galaxies. Hence this result is consistent with previous studies on the consistency between both SFR estimators.

However, the sliding median nearly follows a direct proportionality between $[SFR_{IR}+SFR_{UV}]/SFR_{SED}$ and R_{SB}. The resolved ALMA images offer a nice explanation for this increasing "wrongness" of SFR_{SED} with increasing "starburstiness" by showing a clear offset between the UV and IR light distributions. A galaxy with $R_{SB}\sim4$ forms stars with an intensity nearly 4 times greater than the one derived from SED fitting. This implies that galaxies experiencing a starburst phase may be interpreted as normal MS star-forming galaxies in the absence of direct far-infrared measurements. Equivalently, R_{SB} is a good proxy for the wrongness of SED-derived SFR. This is particularly true in the cases of GS6 and UDF3 for which SFR_{SED} is wrong by a factor 11 and 23 respectively.

We can identify three separate groups of galaxies with an ALMA detection in the SFR_{tot}/SFR_{SED} vs R_{SB} plane. Two groups of galaxies within the upper part of the MS, Gr1 and Gr2, and a third group, Gr3, corresponding to the starbursts ($R_{SB}>3$) of the sample that we already discussed. We now wish to focus on the ALMA galaxies with $R_{SB}<3$ of Gr1 and Gr2.

In a first group, Gr1 in Fig. 16, are the ALMA galaxies that belong to the MS and for which $[SFR_{IR}+SFR_{UV}]/SFR_{SED}<2$. Their images are shown in Fig 8 (except GS8 already discussed in Section 3.1 and Fig. 6). The three color images (right column) show that these galaxies present the shapes of large disks with no obvious sign of disturbance and no strong offset between the UV and IR light. Here the UV and far-infrared light come from the same region consistently with the fact that $[SFR_{IR}+SFR_{UV}]$ and SFR_{SED} are in good agreement, although with a slight offset for UDF13.
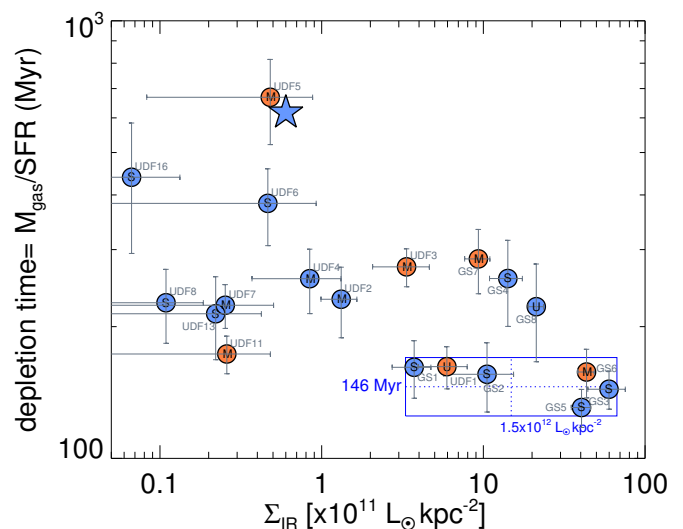
Fig. 17. Depletion time as a function IR luminosity surface density, Σ_{IR}. The blue star shows the typical depletion time of $z\sim2$ MS galaxies (Tacconi et al. 2017).

The second group of galaxies, Gr2, present a $[SFR_{IR}+SFR_{UV}]/SFR_{SED}>3$ ratio typical of starbursts, even though they belong to the MS. These galaxies are discussed in the next section.

### 4.3. Compact starbursts hidden within the main sequence

Surprisingly, galaxies above the MS do not exhibit the largest IR luminosity surface densities. Instead, it is a sub-sample of the galaxies lying within the standard deviation of the MS that experience the most compact star-formation. We discuss the properties of these galaxies in this section, because they appear to be experiencing a peculiar star-formation event that we will demonstrate to be due to a compact starburst *hidden* within the main sequence.

While the depletion time, τ_{dep}, does not change with starburstiness for our small galaxy sample, we do find a trend between τ_{dep} and Σ_{IR}. The typical depletion time for a MS galaxy of $\tau_{dep}\sim600$ Myr (see Section 4.1) is marked with a blue star in Fig. 17. We find that τ_{dep} decreases with Σ_{IR}. The blue rectangle in Fig. 17 identified the galaxies with the shortest τ_{dep} and Σ_{IR}, with median values of $\tau_{dep}=146$ Myr and $\Sigma_{IR}=1.5\times10^{12}$ $L_{\odot}$ kpc^{-2}, or equivalently 255 $M_{\odot}$ yr^{-1} kpc^{-2}. Out of the 6 galaxies located within this zone, only 2 are in a starburst mode (with $R_{SB}>3$, UDF1, GS6, discussed in the previous section), and most are MS galaxies. The images of these MS galaxies experiencing a very efficient and compact mode of star-formation - GS1, GS2, GS3, GS5 - are shown in Fig. 18.

All four MS galaxies turn out to belong also to Gr2 in Fig. 16. Hence they all present a $[SFR_{IR}+SFR_{UV}]/SFR_{SED}>2.5$. A third common point between these galaxies is particularly striking: they all exhibit a strong dichotomy between their IR and UV light distributions (see Fig. 18). This offset explains why SFR_{SED} is a bad proxy for $SFR_{IR}+SFR_{UV}$ for these galaxies. Hence these MS galaxies present equivalent offsets and SFR_{SED} "wrongness" than the "starburst" galaxies lying above the MS, but they belong to the MS. In fact, they do exhibit two important differences with the galaxies lying above the MS.

First, they all exhibit a similar morphology in the *H*-band. They look like face-on disks or alternatively like spheroids. Con-
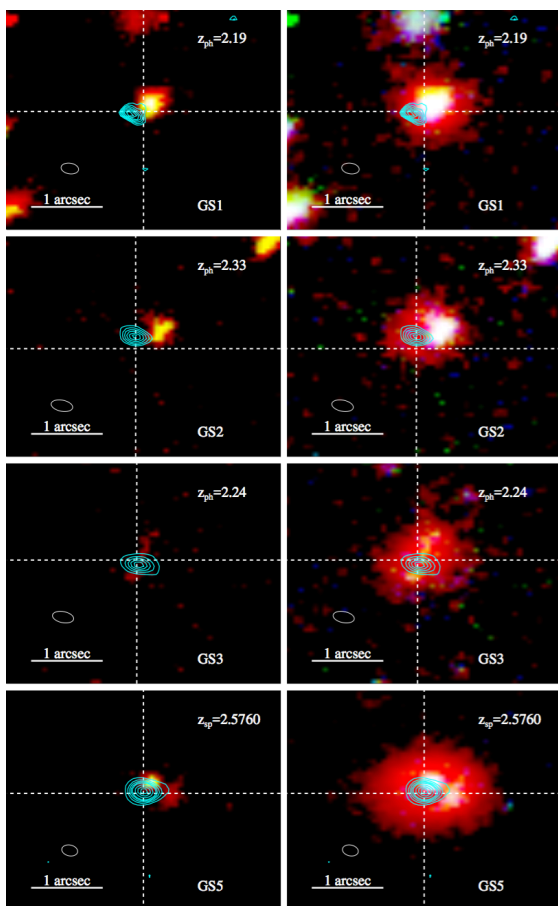
Fig. 18. Same as Fig. 8 for the four MS galaxies with the depletion times of starbursts, ~150 Myr. The starbursts "hidden" in the MS.

sidering that the probability to see these galaxies only face-on is low, we believe that at least some of them are spheroids or will become so. This is at least the case of GS1 with an *H*-band Sérsic index of $n_H^{\mathrm{Sersic}}=3.75$ and possibly also GS3 with $n_H^{\mathrm{Sersic}}=2.03$ and $n_{ALMA}^{\mathrm{Sersic}}=4.7\pm1.7$.

Second, they all have small gas fractions more than twice lower than the galaxies lying above the MS.

Hence we have found evidence for the existence of a population of starbursts, with star formation efficiencies four times greater than MS galaxies at $z\sim2$, hidden *within* the main sequence of star-forming galaxies. These galaxies experience such rapid star formation that they will exhaust their gas reservoirs and stop forming stars in only ~150 Myr. Hence if they are not replenished by diffuse intergalactic matter, these massive galaxies ($M_\star\sim10^{11}$ $M_\odot$) will become passive.

5. The origin of compact starbursts in the main sequence

In a study of six massive, compact, dusty star-forming galaxies at $z\sim2.5$ (including 3 galaxies in common with the present paper), Barro et al. (2016) proposed to explain compact dusty star-forming galaxies as experiencing a phase preceding the formation of a compact early-type galaxy (ETG). The median 5000 Å effective radius (observed *H*-band) of $z\sim2$ massive ($M_\star\sim10^{11}$ $M_\odot$) ETGs is indeed of only 1 kpc whereas the radii of star-forming galaxies in the same mass range is close to 4 kpc (van der Wel et al. 2014). Hence quenching a typical star-

forming galaxy of 4 kpc would not lead to the formation of a 1 kpc compact ETG. The issue of the missing progenitors of the $z\sim2$ compact ETGs would be solved if the compact ALMA sources would stop forming stars and not be replenished by external infall of intergalactic matter. The theoretical explanation favored by Barro et al. (2016) consists in invoking the role of a "wet compaction" event driven during a rapid and massive gas inflow from the surrounding medium, either through cold flows or a series of minor mergers (Zolotov et al. 2015, Tacchella et al. 2016 and references therein). We note however a few caveats to this interpretation.

First, the compact ALMA sources are already massive with observed *H*-band sizes of several kpc and would form typically 30 % of their mass during the event (typically ~450 $M_\odot$ yr^{-1} during ~150 Myr for a ~2×10^{11} $M_\odot$ galaxy), which is not enough to make them as compact as the 1 kpc ETGs. The compact star-forming galaxies identified by Wang et al. (2016) at $z\sim4$ may constitute better candidate progenitors of the compact $z\sim2$ ETGs.

Second, this interpretation requires that the compact star formation event that drives the starburst event is associated with an enhancement of the gas fraction, since it is this large gas flow that would drive the event. In their numerical simulation of dissipation-driven compaction events, Tacchella et al. (2016) "find that the high-SFR galaxies in the upper envelope of the MS are compact, with high gas fractions and short depletion times ('blue nuggets'), while the lower SFR galaxies in the lower envelope have lower central gas densities, lower gas fractions, and longer depletion times". The predicted high gas fractions are also clearly visible in the Fig.4-right of Zolotov et al. (2015) where the gas mass rises rapidly during the compaction event whereas the stellar mass rises more gradually, resulting in a rise of the gas fraction. Instead we show in Fig. 15-right that the galaxies with the most compact star formation exhibit also the lowest gas fractions, in clear contradiction with the prediction of this model. In the framework of the wet compaction hypothesis, star-forming galaxies with low gas fractions would lie in the bottom part of the MS and be less compact, as a successive phase following the gas enhanced compaction phase.

We propose here an alternative explanation for the compact starbursts hidden in the MS exists. These galaxies may represent the late-stage of the major merger of two gas-rich galaxies as in the simulations of Fensch et al. (2017). In these simulations, it is found that while the major merger of two galaxies with 10 % gas fractions do generate strong starbursts with a rise of the SFR by a factor 25, when they consider the merger of two galaxies with 60 % gas fractions, the SFR only rises by a factor 2.5 and only at the late-stage of the merger. The hidden starbursts that we presented in Section 4.3 could be explained by this phase in which the gas fraction has dropped, the SFR has risen without bringing the galaxy above the MS, leading to a short depletion time of only 150 Myr and the morphology is that of a spherical galaxy having lost its disk during the encounter. This would mean that mergers could be playing an important role in both triggering star-formation and transforming disks into spheroids *within* the MS. We note that even in the violent dynamical instability scenario discussed above, the compaction event is in most cases also associated with a merger and rarely happens in isolated galaxies.

We realise that this interpretation leads to another issue: if major mergers do not enhance the SFR of galaxies by more than a factor ~2 in gas-rich galaxies, then why are there some galaxies well above the MS at $z\sim2$? We proposed a solution to this question in Section 4.1, when we noted that the galaxies lying well above the MS exhibited an enhanced gas fraction and that they

systematically appeared to be experiencing a merger. This suggests that what pushes galaxies well above the MS is the infall, during a major merger, of circum-galactic matter. The existence of greater gas contents in galaxies above the MS was already found by Magdis et al. (2012a), accompanied with shorter depletion times. A result confirmed in following studies such as Genzel et al. (2015) and Tacconi et al. (2017). Using ALMA alone as a probe of the molecular gas reservoirs of distant galaxies (without fitting the far-IR bump and determining a dust temperature), Scoville et al. (2016) found only a mild decrease of the depletion time above the MS. They proposed to explain starbursts as gas-rich systems rather than galaxies with more efficient star-formation. However, the fact that starbursts above the MS are also systematically associated (at least in our ALMA sample) with morphological signs of ongoing mergers favors in our opinion the idea that these galaxies are *more efficiently star-forming* if one includes the gas reservoirs at the origin of their enhanced gas fractions. This explanation represents an intermediate position in which starbursts are actually much more efficiently converting gas into stars, if we include the reservoirs of gas responsible for their enhanced gas fractions that must be coming from circum-galactic gas that was not accounted for in the isolated galaxies prior to their merger. This component has until now not been taken into account in simulations of mergers to our knowledge.

6. Conclusions

In this paper, we have presented the properties of a sample of 19 $z\sim2$ star-forming galaxies located in the GOODS-*South* field with high angular resolution imaging and photometry from the UV to the mm range, combining data from the ground, *HST*, *Spitzer*, *Herschel* and ALMA. The ALMA data combine information from deep integrations at $870\,\mu$m on 8 $z\sim2$ sources selected among the brightest *Herschel* sources with data on 11 galaxies coming from a published 1.3 mm survey of the Hubble Ultra-Deep Field, HUDF (Dunlop et al. 2017, Rujopakarn et al. 2016). These galaxies were selected in the high stellar mass range of the star-forming galaxies at $1.5<z<2.5$ in order to include normal star-forming galaxies within the standard deviation of the star formation main sequence, as well as starbursts well above the main sequence.

Our main results are listed below:

1. *Heavily obscured $z\sim2$ massive galaxies:* out of 8 ALMA pointings targeting *Herschel* sources with an optical counterpart at $z\sim2$, one of the ALMA detection presents two properties that led us to identify a background *HST*-dark galaxy as the real *Herschel* and ALMA counterpart. These properties are *(i)* an offset between ALMA and *HST* larger than the astrometric error, *(ii)* a far-IR SED that peaks at $\sim400\,\mu$m. We identified a potential counterpart at a redshift that we estimate to be of $z\sim3.24$. A 67 armcin^2 survey of GOODS-*South* at 1.1mm (P.I. D.Elbaz) appears to confirm the possibility that typically 10-15 % of the ALMA sources are associated with "optically dark" galaxies (Franco et al., in prep.).

2. *Compact star-formation in $z\sim2$ massive galaxies:* while dusty star-formation is resolved in all ALMA galaxies, we find a common point among these massive $z\sim2$ star-forming galaxies: their star formation appears to be concentrated towards the mass center of the galaxies and to be 1.45 ± 1.0 times more compact than at $1.6\,\mu$m, i.e., observed *HST*–WFC3 *H*-band.

3. *Minor contribution of kpc-clumps of star-formation:* kpc-clumps of star formation seen in the UV do not contribute a large fraction of the total star formation rate measured in these massive $z\sim2$ galaxies. This is consistent with the small SFR attributed to the giant UV clumps (see Elmegreen et al. 2009). In one case, we see marginal evidence for the ALMA detection of a kpc-clump.

4. *The IR8 color index as a probe of star-formation compactness:* we present an updated version of the *IR*8-Σ_{IR} relation (introduced in Elbaz et al. 2011) for local galaxies, now including resolved *Herschel* images for local galaxies, and discuss its extension to $z\sim2$. The *IR*8 color index (=L_{IR}/L_8) and the IR luminosity surface density, Σ_{IR} (a proxy for the dusty star formation density) present a tight correlation for local galaxies with a standard deviation of only *rms*=0.11 dex. The $z\sim1.5$-2.5 galaxies resolved with ALMA appear to follow the local relation, although galaxies both *within* and *above* the main sequence can exhibit high Σ_{IR} values.

5. *A connection between AGN activity and star-formation compactness:* galaxies hosting an AGN appear to be outliers to the *IR*8-Σ_{IR} relation both locally and at $z\sim2$. While a correction of the contribution of hot dust continuum due to AGN heating may explain in part or possibly completely the position of these galaxies, by lowering their *IR*8, galaxies hosting an AGN are found to be systematically associated with the most compact star-forming galaxies. This suggests that the mechanism responsible for the most compact star-forming galaxies also switches on the AGN, or possibly that the AGN plays a role in triggering the compact star-formation through positive feedback (see e.g., Silk 2013, Molnár et al. 2017, Elbaz et al. 2009).

6. *On the origin of merger-driven starbursts above the star formation main sequence:* galaxies above the SFR-M$_\star$ main sequence systematically exhibit the visual morphology of perturbed galaxies as expected in the case of major mergers. However, their enhanced SFR neither appears to be associated with a drop in depletion time, hence enhanced star formation efficiency, nor with a rise of star formation compactness. Instead we find a systematic increase of the gas mass fraction in these galaxies. Assuming that this effect is not artificially created by a larger metallicity in starbursts, which would lead to an overestimate of their gas content, this increase in gas content may be explained by the infall of circum-galactic material induced during the merger. Hydrodynamical simulations accounting for this effect do not presently exist to our knowledge and should be performed to test this hypothesis.

7. *SFR derived from SED-fitting underestimates the SFR with increasing "starburstiness":* we present a near proportionality between the ratio of SFR$_{tot}$ (=SFR$_{IR}$+SFR$_{UV}$) over SFR$_{SED}$ (determined by fitting the rest-frame UV-optical-NIR) and the distance to the main sequence or starburstiness (R$_{SB}$=SFR$_{tot}$/MS). The sources of rest-frame UV and far-IR emission in starbursts occupy very distinct locations. Both properties – the high SFR$_{tot}$/SFR$_{SED}$ and different locations of UV and IR – are natural consequences of the presence of highly obscured star formation in these galaxies.

8. *Highly obscured star formation within the main sequence:* we find evidence for highly obscured star-formation also associated with a spatial offset between UV and far-IR light distributions in a sub-population of main sequence galaxies. These galaxies experience compact starbursts.

9. *Compact "starbursts" within the main sequence:* we find that the depletion time, τ_{dep} (the time for a galaxy to consume its

molecular gas reservoir), drops with increasing IR luminosity surface density, Σ_{IR}. A sub-population of galaxies form stars with the shortest τ_{dep} and highest Σ_{IR} with median values of τ_{dep}=146 Myr and Σ_{IR}=1.5$\times10^{12}$ L$_{\odot}$ kpc^{-2}. These galaxies being dominantly located in the upper part of the main sequence, they are starbursts "hidden" within the main sequence. Like starbursts above the main sequence, their UV and far-IR light exhibit very distinct spatial distributions and their SFR$_{tot}$ are much larger than their SFR$_{SED}$. Their morphologies are however very different: they show no clear sign of perturbation and present a rather circular morphology, suggesting that they may be bulges in formation. They also have low gas fraction, as opposed to the starburst above the main sequence which all show enhanced gas fractions. Hence we believe that they have a different origin.

10. *Physical origin of the compact starbursts within the main sequence:* the compact starbursts hidden in the main sequence may be late-stage mergers of gas-rich galaxies. High-resolution simulations have indeed shown that major mergers of gas-rich galaxies only mildly affect the proportion of dense gas in galaxies, and hence their star formation rate (Fensch et al. 2017). It is only in the late-stage of the merger of gas-rich galaxies (60 %) that the SFR rises by about ×2.5, while it rises by typically ×25 in gas poor (10 %) galaxies. If this interpretation is correct, this would mean that mergers do affect star formation and the morphological transformation of galaxies *within* the main sequence and not only among the "starbursts" well above the main sequence. We discussed the alternative explanation proposed by several papers (Barro et al. 2016, Zolotov et al. 2015, Tacchella et al. 2016) that the compact star-formation in main sequence galaxies is associated with a "compaction" event due to a violent dynamical instability of gas-rich galaxies under the effect of large infall of extragalactic matter. However, we note that the galaxies discussed here exhibit a low gas fraction, while this scenario has been described as being associated with enhanced gas fractions. We also note that even in the instability scenario, the compaction events described in those studies are in most cases also associated with a merger event and rarely happen in isolated galaxies.

References

Abel, N. P., Dudley, C., Fischer, J., Satyapal, S., & van Hoof, P. A. M. 2009, ApJ, 701, 1147
Allamandola, L. J., Tielens, A. G. G. M., & Barker, J. R. 1985, ApJ, 290, L25
Armus, L., Mazzarella, J. M., Evans, A. S., et al. 2009, PASP, 121, 559
Barro, G., Kriek, M., Pérez-González, P. G., et al. 2016, ApJ, 827, L32
Béthermin, M., Daddi, E., Magdis, G., et al. 2015, A&A, 573, A113
Brammer, G. B., van Dokkum, P. G., & Coppi, P. 2008, ApJ, 686, 1503
Bruzual, G. & Charlot, S. 2003, MNRAS, 344, 1000
Buat, V., Noll, S., Burgarella, D., et al. 2012, A&A, 545, A141
Burgarella, D., Buat, V., Gruppioni, C., et al. 2013, A&A, 554, A70
Calzetti, D., Armus, L., Bohlin, R. C., et al. 2000, ApJ, 533, 682

Chambers, K. C., Magnier, E. A., Metcalfe, N., et al. 2016, ArXiv e-prints [arXiv:1612.05560]
Chang, Y.-Y., Le Floc'h, E., Juneau, S., et al. 2017, ArXiv e-prints [arXiv:1711.00471]
Chary, R. & Elbaz, D. 2001, ApJ, 556, 562
Cibinel, A., Daddi, E., Bournaud, F., et al. 2017, MNRAS, 469, 4683
Cowie, L. L., Hu, E. M., & Songaila, A. 1995, AJ, 110, 1576
Daddi, E., Bournaud, F., Walter, F., et al. 2010a, ApJ, 713, 686
Daddi, E., Cimatti, A., Renzini, A., et al. 2004, ApJ, 617, 746
Daddi, E., Dannerbauer, H., Liu, D., et al. 2015, A&A, 577, A46
Daddi, E., Dickinson, M., Morrison, G., et al. 2007, ApJ, 670, 156
Daddi, E., Elbaz, D., Walter, F., et al. 2010b, ApJ, 714, L118
Díaz-Santos, T., Armus, L., Charmandaris, V., et al. 2017, ArXiv e-prints [arXiv:1705.04326]
Díaz-Santos, T., Charmandaris, V., Armus, L., et al. 2010, ApJ, 723, 993
Donley, J. L., Koekemoer, A. M., Brusa, M., et al. 2012, ApJ, 748, 142
Draine, B. T., Dale, D. A., Bendo, G., et al. 2007, ApJ, 663, 866
Draine, B. T. & Li, A. 2007, ApJ, 657, 810
Dunlop, J. S., McLure, R. J., Biggs, A. D., et al. 2017, MNRAS, 466, 861
Elbaz, D., Daddi, E., Le Borgne, D., et al. 2007, A&A, 468, 33
Elbaz, D., Dickinson, M., Hwang, H. S., et al. 2011, A&A, 533, A119
Elbaz, D., Hwang, H. S., Magnelli, B., et al. 2010, A&A, 518, L29
Elbaz, D., Jahnke, K., Pantin, E., Le Borgne, D., & Letawe, G. 2009, A&A, 507, 1359
Elmegreen, B. G., Bournaud, F., & Elmegreen, D. M. 2008, ApJ, 688, 67
Elmegreen, B. G. & Elmegreen, D. M. 2005, ApJ, 627, 632
Elmegreen, B. G., Elmegreen, D. M., Fernandez, M. X., & Lemonias, J. J. 2009, ApJ, 692, 12
Erb, D. K., Shapley, A. E., Pettini, M., et al. 2006, ApJ, 644, 813
Erwin, P. 2015, ApJ, 799, 226
Fensch, J., Renaud, F., Bournaud, F., et al. 2017, MNRAS, 465, 1934
Flewelling, H. A., Magnier, E. A., Chambers, K. C., et al. 2016, ArXiv e-prints [arXiv:1612.05243]
Fontana, A., Dunlop, J. S., Paris, D., et al. 2014, A&A, 570, A11
Fujimoto, S., Ouchi, M., Shibuya, T., & Nagai, H. 2017, ArXiv e-prints [arXiv:1703.02138]
Genzel, R., Tacconi, L. J., Combes, F., et al. 2012, ApJ, 746, 69
Genzel, R., Tacconi, L. J., Lutz, D., et al. 2015, ApJ, 800, 20
Guo, Y., Ferguson, H. C., Giavalisco, M., et al. 2013, ApJS, 207, 24
Heinis, S., Buat, V., Béthermin, M., et al. 2013, MNRAS, 429, 1113
Hodge, J. A., Swinbank, A. M., Simpson, J. M., et al. 2016, ApJ, 833, 103
Hopkins, P. F., Bundy, K., Croton, D., et al. 2010, ApJ, 715, 202
Karim, A., Schinnerer, E., Martínez-Sansigre, A., et al. 2011, ApJ, 730, 61
Kartaltepe, J. S., Dickinson, M., Alexander, D. M., et al. 2012, ApJ, 757, 23
Kartaltepe, J. S., Sanders, D. B., Scoville, N. Z., et al. 2007, ApJS, 172, 320
Kennicutt, Jr., R. C. 1998, ApJ, 498, 541
Kriek, M., van Dokkum, P. G., Labbé, I., et al. 2009, ApJ, 700, 221
Le Floc'h, E., Papovich, C., Dole, H., et al. 2005, ApJ, 632, 169
Leger, A. & Puget, J. L. 1984, A&A, 137, L5
Leiton, R., Elbaz, D., Okumura, K., et al. 2015, A&A, 579, A93
Leroy, A. K., Bolatto, A., Gordon, K., et al. 2011, ApJ, 737, 12
Luo, B., Brandt, W. N., Xue, Y. Q., et al. 2017, ApJS, 228, 2
Madau, P. & Dickinson, M. 2014, ARA&A, 52, 415
Magdis, G. E., Daddi, E., Béthermin, M., et al. 2012a, ApJ, 760, 6
Magdis, G. E., Daddi, E., Sargent, M., et al. 2012b, ApJ, 758, L9
Magnelli, B., Elbaz, D., Chary, R. R., et al. 2009, A&A, 496, 57
Magnelli, B., Popesso, P., Berta, S., et al. 2013, A&A, 553, A132
Meurer, G. R., Heckman, T. M., & Calzetti, D. 1999, ApJ, 521, 64
Molnár, D. C., Sargent, M. T., Elbaz, D., Papadopoulos, P. P., & Silk, J. 2017, MNRAS, 467, 586
Mullaney, J. R., Alexander, D. M., Goulding, A. D., & Hickox, R. C. 2011, MNRAS, 414, 1082
Noeske, K. G., Weiner, B. J., Faber, S. M., et al. 2007, ApJ, 660, L43
Noll, S., Burgarella, D., Giovannoli, E., et al. 2009, A&A, 507, 1793
Overzier, R. A., Heckman, T. M., Wang, J., et al. 2011, ApJ, 726, L7
Pannella, M., Carilli, C. L., Daddi, E., et al. 2009, ApJ, 698, L116
Pannella, M., Elbaz, D., Daddi, E., et al. 2015, ApJ, 807, 141
Peng, C. Y., Ho, L. C., Impey, C. D., & Rix, H.-W. 2002, AJ, 124, 266
Puglisi, A., Daddi, E., Renzini, A., et al. 2017, ApJ, 838, L18
Reddy, N., Dickinson, M., Elbaz, D., et al. 2012, ApJ, 744, 154
Renzini, A. & Peng, Y.-j. 2015, ApJ, 801, L29
Rodighiero, G., Daddi, E., Baronchelli, I., et al. 2011, ApJ, 739, L40
Rodighiero, G., Renzini, A., Daddi, E., et al. 2014, MNRAS, 443, 19
Rujopakarn, W., Dunlop, J. S., Rieke, G. H., et al. 2016, ApJ, 833, 12
Rujopakarn, W., Rieke, G. H., Eisenstein, D. J., & Juneau, S. 2011, ApJ, 726, 93
Salpeter, E. E. 1955, ApJ, 121, 161
Schreiber, C., Pannella, M., Elbaz, D., et al. 2015, A&A, 575, A74
Schreiber, C., Pannella, M., Leiton, R., et al. 2017, A&A, 599, A134
Scoville, N., Sheth, K., Aussel, H., et al. 2016, ApJ, 820, 83
Shivaei, I., Reddy, N. A., Shapley, A. E., et al. 2017, ApJ, 837, 157
Silk, J. 2013, ApJ, 772, 112
Silverman, J. D., Daddi, E., Rodighiero, G., et al. 2015, ApJ, 812, L23
Tacchella, S., Dekel, A., Carollo, C. M., et al. 2016, MNRAS, 457, 2790
Tacconi, L. J., Genzel, R., Neri, R., et al. 2010, Nature, 463, 781
Tacconi, L. J., Genzel, R., Saintonge, A., et al. 2017, ArXiv e-prints [arXiv:1702.01140]
Tadaki, K.-i., Genzel, R., Kodama, T., et al. 2017, ApJ, 834, 135
van der Wel, A., Bell, E. F., Häussler, B., et al. 2012, ApJS, 203, 24
van der Wel, A., Franx, M., van Dokkum, P. G., et al. 2014, ApJ, 788, 28
Wang, T., Elbaz, D., Schreiber, C., et al. 2016, ApJ, 816, 84
Whitaker, K. E., Franx, M., Leja, J., et al. 2014, ApJ, 795, 104
Whitaker, K. E., van Dokkum, P. G., Brammer, G., & Franx, M. 2012, ApJ, 754, L29
Wuyts, S., Förster Schreiber, N. M., Lutz, D., et al. 2011a, ApJ, 738, 106
Wuyts, S., Förster Schreiber, N. M., van der Wel, A., et al. 2011b, ApJ, 742, 96
Zolotov, A., Dekel, A., Mandelker, N., et al. 2015, MNRAS, 450, 2327